van Genuchten, C.M.; Hopwood, M.J.; Liu, T.; Krause, J.; Achterberg, E.P.; Rosing, M.T.; Meire, L. (2022). Solid-phase Mn speciation in suspended particles along meltwater-influenced fjords of West Greenland. *Geochim. Cosmochim. Acta 326*: 180-198. DOI: 10.1016/j.gca.2022.04.003

Published version: https://dx.doi.org/10.1016/j.gca.2022.04.003

NIOZ Repository: http://imis.nioz.nl/imis.php?module=ref&refid=352035

Solid-phase Mn speciation in suspended particles along meltwater-influenced fjords of West Greenland

C. M. van Genuchten[1], M. J. Hopwood[2,3], T. Liu[2], J. Krause[2], E. P. Achterberg[2], M. T. Rosing[4], L. Meire[5,6]

[1]Department of Geochemistry, Geological Survey of Denmark and Greenland, Copenhagen, Denmark

[2]GEOMAR Helmholtz Centre for Ocean Research Kiel, Kiel, Germany

[3]Department of Ocean Science and Engineering, Southern University of Science and Technology, Shenzhen, China

[4]Globe Institute, University of Copenhagen, Copenhagen, Denmark

[5]Greenland Climate Research Centre, Greenland Institute of Natural Resources, Nuuk, Greenland

[6]Department of Estuarine and Delta Systems, Royal Netherlands Institute for Sea Research, Yerseke, The Netherlands

Abstract

Manganese (Mn) is an essential micro-nutrient that can limit or, along with iron (Fe), co-limit phytoplankton growth in the ocean. Glacier meltwater is thought to be a key source of trace metals to high latitude coastal systems, but little is known about the nature of Mn delivered to glacially-influenced fjords and adjacent coastal waters. In this work, we combine in-situ dissolved Mn (dMn) measurements of surface waters with Mn K-edge X-ray absorption spectroscopy (XAS) data of suspended particles in four fjords of West Greenland. Data were collected from transects of up to 100 km in fjords with different underlying bedrock geology from 64 to 70°N. We found that dMn concentrations generally decreased conservatively with increasing salinity (from 80-120 nM at salinity <8 to <40 nM at salinities >25). Dissolved Fe (dFe) trends in these fjords similarly declined with increasing distance from glacier outflows (declining from >20 nM to <8 nM). However, the dMn/dFe ratio increased rapidly likely due to the greater stability of dMn at intermediate salinities (i.e. 10 – 20) compared to rapid precipitation of dFe across the salinity gradient. The XAS data indicated a widespread presence of Mn(II)-rich suspended particles near fjord surfaces, with structures akin to Mn(II)-bearing phyllosilicates. However, a distinct increase in Mn oxidation state with depth and the predominance of birnessite-like Mn(IV) oxides was observed for suspended particles in a fjord with tertiary basalt geology. The similar dMn behaviour in fjords with different suspended particle Mn speciation (i.e., Mn(II)-bearing phyllosilicates and Mn(IV)-rich birnessite) is consistent with the decoupling of dissolved and particulate Mn and suggests that dMn concentrations on the scale of these fjords are controlled primarily by dilution of a freshwater dMn source rather than exchange between dissolved and particle phases. This work provides new insights into the Mn cycle in high latitude coastal waters, where small changes in the relative

availabilities of dMn, dFe and macronutrients may affect the identity of the nutrient(s) proximally limiting primary production.

1. Introduction

Manganese (Mn) is an essential micro-nutrient for all known photosynthetic organisms (Morel and Price, 2003) because it is integral to water oxidation in photosystem II and can serve as a co-factor in key enzymes, including Mn superoxide dismutase (Peers and Price, 2004; Hansel, 2017). Due to its importance for phytoplankton metabolism, Mn can limit or co-limit marine phytoplankton growth (Pausch et al., 2019). For example, Mn concentrations are depleted in parts of the offshore Southern Ocean (Latour et al., 2021) and recent work suggests Mn- or Fe/Mn co-limitation is prevalent in Drake Passage (Browning et al., 2021). Concentrations of dMn are generally much higher in coastal Arctic and high latitude North Atlantic environments around Greenland (Colombo et al., 2020; Achterberg et al., 2021; Krisch et al., 2021) and thus unlikely to limit marine primary production, but Mn cycling may nevertheless influence other biogeochemical cycles. Mn oxides are for example a strong scavenger of dissolved cobalt in the ocean (Hawco et al., 2018).

Although atmospheric particle fluxes are a major trace metal source to oceans on a global scale (Boyd and Ellwood, 2010), recent work suggests particle-rich glacier meltwater and the associated shelf sediments can be significant regional sources of Mn and Fe along glaciated coastlines (Wehrmann et al., 2014; Hawkings et al., 2020; Forsch et al., 2021). Glacially-derived metal fluxes are expected to be particularly prominent in glaciated fjords, such as along the coastline of West Greenland, where meltwater is confined, creating strong gradients in turbidity and salinity (Hopwood et al., 2016). Since the annual meltwater flux from the Greenland Ice

Sheet is expected to increase in the future due to increasing Arctic air temperatures (Boers and Rypdal, 2021; Slater et al., 2021), glacially-sourced Mn (and Fe) inputs may increase. However, the flux and speciation of Mn, particularly solid-phase Mn, delivered to fjords and adjacent waters are poorly understood. Addressing the knowledge gap concerning how solid-state speciation affects the exchange of metals between the solid and dissolved phases is particularly important for understanding potential changes in metal availability to marine ecosystems, where cellular acquisition of trace elements primarily occurs from dissolved phases.

In the environment, Mn can exist in three oxidation states, each with unique reactivity and different roles in the oceanic cycles of other elements. Divalent Mn (Mn(II)), one of the most bioavailable Mn forms, is often a major fraction of dissolved Mn (dMn) in aquatic environments (Jones et al., 2020). Mn(II) is more soluble than oxidized Mn (Jones et al., 2020) and is relatively stable in oxic environments. For example, homogeneous Mn(II) oxidation by O_2 to form particulate Mn oxides requires months to years (Diem and Stumm, 1984). Abiotic Mn(II) oxidation by O_2 can be catalysed by mineral surfaces, but Mn(II) is still relatively stable in the presence of surfaces, with a reported half-life on the order of days (Davies and Morgan, 1989; Morgan, 2005). Consequently, Mn(II) oxidation rates in the marine environment are thought to be largely controlled by microorganisms rather than inorganic processes (Tebo and Emerson, 1986; Sunda and Huntsman, 1987) because biotic Mn(II) oxidation can be several orders of magnitude faster than abiotic oxidation (Tebo et al., 2004; Learman et al., 2011). Microbial-mediated Mn(II) oxidation is typically initiated by the biotic generation of reactive oxygen species (ROS), such as the superoxide radical (Learman et al., 2013), though ROS can also form abiotically (Nico et al., 2002). The vertical distribution of dMn in the ocean is characterised by high surface concentrations of dMn(II) (4 – 10 nM) due to photoreduction of Mn(III/IV) oxides and photoinhibition of microbial Mn(II) oxidation (Sunda et al., 1983; Sunda and Huntsman, 1988; Colombo et al., 2020). This produces a distinct surface dMn maxima and generally contrasts with the distribution of most other bio-active trace elements which show mid-water column maxima due to surface drawdown and subsurface remineralization (Sunda, 2012). Although moderately soluble, Mn(II) can also be present in the solid phase, with Mn(II)-bearing carbonates and aluminosilicates reported in estuarine and ocean sediments (Lenz et al., 2014; Yu et al., 2016).

Trivalent Mn (Mn(III)) is unstable in solution and disproportionates rapidly. Therefore, stable Mn(III) is often found associated with particles as a minor species bound to metal oxides or silicates (Carroll et al., 2002; Ling et al., 2018) or more rarely as a separate Mn(III) oxide (Ostwald and Frazer, 1973). However, organic ligands can also stabilize dissolved Mn(III), with recent studies suggesting that Mn(III)-ligand complexes can dominate dMn in waters with high dissolved organic carbon concentrations (Oldham et al., 2020). Since Mn(III) can both accept and donate electrons, it can participate in many oceanic element redox cycles.

Tetravalent Mn(IV) is found primarily in the solid phase, typically formed via biogenic Mn(II) oxidation to create nanoscale Mn(IV) oxides that have unique redox and sorption properties (Tebo et al., 2004). Mn(IV) oxides are some of the ocean's most powerful oxidants and can rapidly oxidize key redox-active species, including cobalt and organic carbon (Wang and Stone, 2006; Simanova and Pena, 2015). The strong metal sorption reactivity of Mn(IV) oxides, such as biogenic birnessite, has earned them the reputation as the "scavengers of the sea" (Goldberg, 1954). However, Mn(IV) is also unstable in sunlight and is photoreduced readily to Mn(II,III) (Sunda et al., 1983).

Since the biogeochemical reactivity of Mn evidently depends on its oxidation state, knowledge of particulate Mn speciation, and how it relates to dMn, is essential to understand the impact of glacier-sourced material on Mn availability in coastal waters. However, most studies employ an operational definition of solid-phase Mn based exclusively on filtration using different filter pore sizes or acid digestions (Evans and Nishioka, 2018; Jensen et al., 2020; Forsch et al., 2021). Although helpful, simple distinction between different sizes of particulate Mn is not an ideal approach because it cannot unambiguously distinguish some different Mn-bearing solids that have dramatically different reactivities. One of the barriers to a more detailed understanding of particulate Mn speciation is that traditional mineralogical tools are often inadequate to characterize particulate Mn because the Mn content of suspended particles can be too dilute and the Mn-bearing solid can be poorly-ordered and lacking Bragg peaks in X-ray diffraction (Webb et al., 2005). However, advancements at synchrotron facilitates have improved access to sophisticated fluorescence yield detectors that, when coupled to an element-specific technique like X-ray absorption spectroscopy (XAS), can routinely measure the solid-phase speciation of dilute metals in environmental matrices (Proux et al., 2017; Lefebvre et al., 2021; Xiang et al., 2021). Therefore, in combination with dMn data, synchrotron-based XAS can be a pivotal tool to unravel the complex behaviour of particulate Mn in dynamic environmental contexts, such as marine regions affected by glacier discharge.

In this work, we integrate measurements of in-situ dMn concentrations with synchrotron-based Mn K-edge XAS data of suspended particles in four West Greenland fjords separated by hundreds of km. Data were collected from transects of up to 100 km in length in fjords with different underlying bedrock geology. The Mn data are also contrasted with Fe data from the same transects, which was first presented in our previous work (van Genuchten et al., 2021), and evaluated in view of other reported Mn datasets in similar geographic environments around Greenland (Aciego et al., 2015; Hawkings et al., 2020; Achterberg et al., 2021; Krisch et al., 2021). These results provide insights into the biogeochemical behaviour of glacially-derived Mn and may help refine predictions concerning future changes to the relative availabilities of Fe and Mn in glaciated coastal regions (Browning et al., 2021; Forsch et al., 2021).

2. Methods

2.1 Sampling locations

Four transects in West Greenland were sampled (Figure 1, Figure S1 for satellite images) all close to the expected peak of the annual meltwater season. Runoff (i.e. liquid discharge) has only been monitored continuously through the meltwater season in situ at a handful of sites around Greenland, but modelled data products along the West Greenland coastline suggest runoff is a continuous flow by May and reaches peak values in July or August before declining into September (Mankoff et al., 2020). Two of the transects were conducted in Ameralik and the neighbouring Godthåbsfjord (Nuup Kangerlua), which are both located in southwest Greenland near Nuuk (Figure 1A). Ameralik (AM) and Godthåbsfjord (GHF) are situated in the Archaean Block of West Greenland, with a geology dominated by Tonalite-Trondhjemite-Granodiorite gneiss, but with significant mafic, ultramafic and metasedimentary components (Naeraa et al., 2014). The AM transect was sampled during two separate research cruises with RV Avataq in August 2019 for fjord water sampling and in June 2015 for suspended particle sampling. The GHF transect was performed in July 2019 using RV Avataq, with a series of depth-resolved suspended particle samples (including sediment from calved ice) also collected from a single location (64°38’ N, 50°09’ W) near the Narsap Sermia glacier terminus (Figure 1) in a separate research cruise in June 2015. While subsets of the AM and GHF transect data were collected in different years, all data were collected in the summer and the particle geology is not likely to change considerably on this timescale. An additional sample collected from the Nuuk area was a dry glacially-abraded rock flour material obtained directly from a raised seabed deposit 15 km north of Nuuk (64°17’ N, 51°43’ W; striped square in Figure 1A).

The other two transects were performed in the Disko Bay region in July 2019 with RV Sanna (Figure 1B and 1C). One transect was performed in the Disko Fjord, which is a ~50 km long fjord located in the southwest of Disko Island. This transect is herein referred to as the Disko Island (DI) transect. The geology of Disko Island (Qeqertarsuaq) consists of tertiary basalt flows and sills overlying Precambrian felsic basement (Mascarenhas and Zielinski, 2019). Another transect was conducted in Arfersiorfik Fjord, a large fjord over 100 km in length that lies south of the town of Aasiaat and north of Nordre Strømfjord (Nassuttooq Fjord). This transect is herein referred to as the Arfersiorfik (AF) transect. The geology of the Greenland coast for the AF transect is characterized by Precambrian basement consisting primarily of amphibolite – granulite facies gneisses (Mascarenhas and Zielinski, 2019). The vast majority of all glaciers in the studied catchment areas are land terminating glaciers, with the only exception being GHF, which hosts three marine-terminating and three land-terminating glaciers.

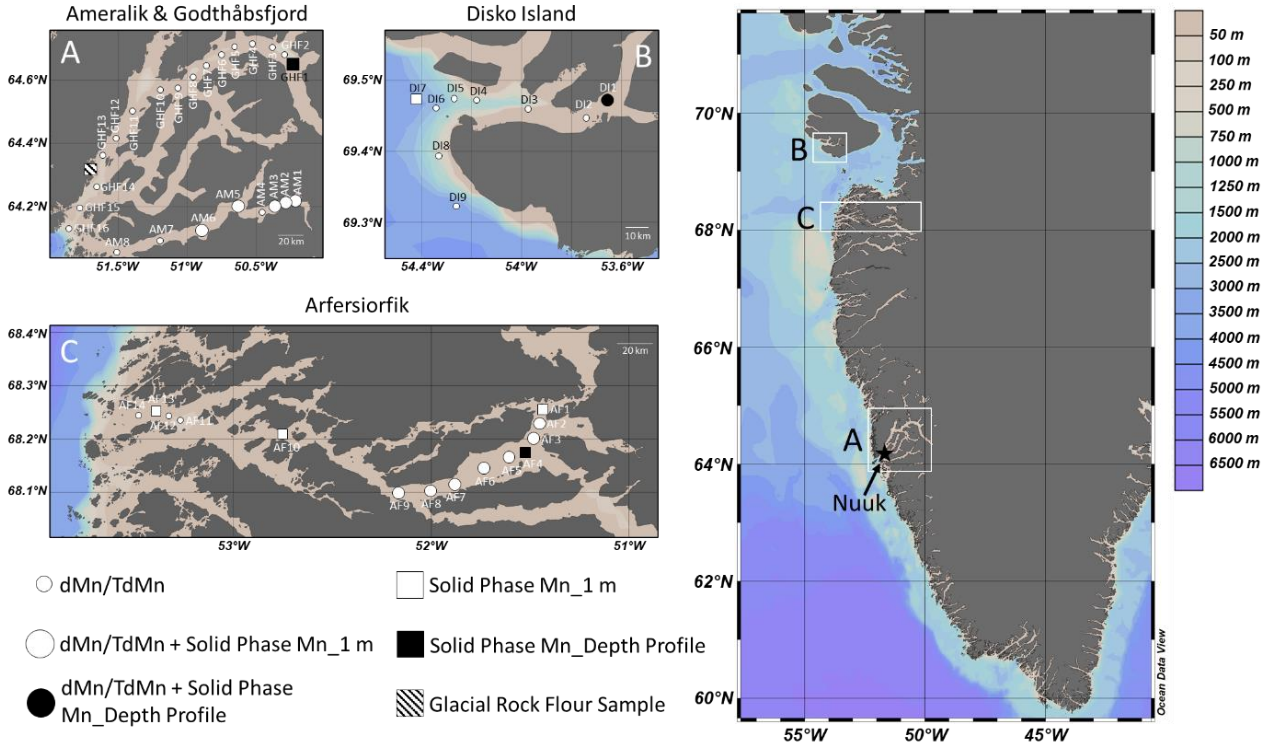

Figure 1: Map of West Greenland sampling locations for the Ameralik (AM), Godthåbsfjord (GHF), Disko Island (DI) and Arfersiorfik (AF) transects. The colour contours indicate ocean bathymetry (General Bathymetric Chart of the Oceans). Maps were produced with Ocean Data View (Schlitzer, 2014). The GHF ice sample was collected in the same area as the GHF depth profile (black square in panel A). dMn and TdMn symbols indicate sampling positions of dissolved and total dissolvable Mn, respectively. Solid Phase Mn_1 m and Solid Phase_Depth Profile refer to suspended particle samples taken at 1 m depth and in depth profiles, respectively.

2.2. Sampling procedures

Fjord water was collected for measurements of dMn at ~1 m depth with acid-cleaned high density polyethylene (HDPE) bottles fitted to a HydroBios sampler on a nylon line (AM and GHF) or by using a custom made towfish device (DI and AF). For AM and GHF, samples were filtered through 0.2 µm Millipore polyvinyl difluoride syringe filters, which were flushed with 0.1 M HCl, ultrapure water (18.2 MΩ·cm MilliQ) and sample water before use. For DI and AF samples, the towfish was mounted on a winch ~2 m away from the ship's hull when underway and was operated by continuously pumping water with a polytetrafluoroethylene

(PTFE) diaphragm pump (Dellmeco, DM15) through polyvinyl chloride (PVC) tubing (pre-cleaned with 0.1 M HCl). The towfish was equipped with an inline filtration system (AcroPak pre-filter with 0.8 µm pore size followed by second filter with 0.2 µm pore size; polyethersulfone filters) to filter water samples. Trace metal clean 125 mL low density polyethylene (LDPE, Nalgene) bottles were used to retain filtered water. A three-stage washing procedure (1 day in detergent, 1 week in 2 M HCl, 1 week in 2 M HNO_3 with three to five rinses of ultrapure water after each stage) was used to prepare the LDPE bottles in advance. The bottles were stored empty and double bagged until use. Filtered samples were acidified to pH <2.0 by the addition of 180 µL HCl (Romil Ultrapure grade acid, part-per-trillion level impurities) within 2 days of sample collection and stored upright for at least 6 months prior to analysis. A subset of samples from AM and GHF transects was retained without filtration and acidified as above in order to determine total dissolvable Mn (TdMn). A laminar flow hood was used for sample processing on-board the ship.

For dMn analysis, samples were preconcentrated using a Preplab device (PS Analytical) and analysed via inductively coupled plasma mass spectrometry (ICP-MS, ThermoFisher Element XR) at GEOMAR. To provide a comparison with dMn concentrations, we also report dissolved Fe (dFe) concentrations from the same samples, which were first presented in our previous companion article (van Genuchten et al., 2021). Other trace element concentrations (dissolved Cu, Co and Ni) are reported by Krause et al., (2021) from the same samples and method as per dFe. The dFe concentrations were analysed with preconcentration offline using a seaFAST system as per Rapp et al. (2017). After standing acidified for >6 months, TdMn samples were measured via ICP-MS following 5 to 50 times dilution with 1 M HNO_3 to account for the large concentration range (distilled in-house from Romil Superpure grade acid, parts-perbillion level impurities). The accuracy of the dMn measurements was determined from analysis of coastal seawater GSC (GEOTRACES Program) and CASS6 (National Research Council Canada) reference material (measured 2.49 ± 0.84 nM and 37.1 ± 0.83 nM; reference values 2.18 ± 0.075 nM and 40.4 ± 2.18 nM, corresponding to recoveries of 114% and 92%, respectively; dFe values are given in our previous work (van Genuchten et al., 2021)). The limit of detection, defined as 3 standard deviations of blanks, was 64 pM for dMn.

Where possible, fjord samples were collected in combination with physical data, which included salinity and temperature (i.e., CTD data) from ~1 m depth. These CTD data are reported alongside dMn data. When and where CTD data were not measured alongside dMn sampling, a handheld LF 325 conductivity meter (WTW) was used to record in-situ temperature and salinity.

Suspended particle samples were collected at depths from 1 to 300 m using a 5 L Go-Flo bottle that was separated from a stainless steel cable by a nylon line to minimize contamination from the cable. For these samples, the fjord water was filtered immediately after collection aboard the ship using a vacuum pump with 0.2 µm polyethersulfone (PES) disk filters (25 mm diameter; Sartorius). Although the filter membranes for collection of suspended particles and dMn samples were different materials, the approximate filter pore size was identical and, in any case, clogging of any filter by collection of sufficient material for beamtime analysis will attenuate the effective pore-size. For each sample location and depth, approximately 1-2 L of the suspension was filtered (or less if the filter clogged). The disk filters with retained solids were then sealed in air-tight petri dishes while still wet and kept frozen throughout the cruise (stored in -80° C freezer) and during shipment to the home institute (packed with dry ice).

2.3 X-ray absorption spectroscopy

2.3.1 Data collection

Suspended sediment samples were analysed by Mn K-edge X-ray absorption spectroscopy (XAS) at beam line 4-1 of the Stanford Synchrotron Radiation Lightsource (SSRL; Menlo Park, USA). Data were collected in fluorescence mode out to a maximum of $k = 12$ Å^{-1} using a 30-element solid state Ge detector (Canberra), with the samples housed in a liquid nitrogen cryostat (77 K) during data collection. Individual scans for each sample were compared and no beam damage was observed. Spectra were aligned, averaged and background-subtracted using SixPack software following a previous approach (van Genuchten and Pena, 2017).

2.3.2. Mn K-edge X-ray absorption near-edge structure (XANES) analysis

The average Mn oxidation state (AMOS) of the samples was determined using linear combination fits (LCFs) following the Combo method, which is described in detail elsewhere (Manceau et al., 2012). The LCFs were performed from 6535 to 6575 eV using the SixPack software (Webb, 2005). The sum of the reference spectra components in the LCFs was not constrained to 1.0 and negative components were not allowed. Each of the Mn-bearing references used in the Combo method LCFs are plotted in Figure S2 in the Supplementary Materials (SM).

2.3.3. Mn K-edge extended X-ray absorption fine structure (EXAFS) analysis

Principal component analysis of EXAFS spectra with adequate data quality (>20 samples) was performed with SixPack software (Webb, 2005). The number of independent components that reproduced the major variance of the EXAFS dataset was determined by minimizing the indicator function (IND) (Malinowski, 1977).

The local Mn bonding environment of select reference materials, which were collected partly in our previous work (van Genuchten and Pena, 2017), and suspended particle samples was determined by shell-by-shell fits of the Fourier-transformed EXAFS spectra. The fits were performed with algorithms derived from IFEFFIT (Newville, 2001) over the range of 1 to 3.5 Å in R+ΔR-space, which was selected to ensure the second-nearest-neighbour atom could be identified (i.e. Mn-Mn), though we acknowledge fits of higher order atomic shells would yield additional information. Since the presence of multiple Mn oxidation states and bonding environments complicates shell-by-shell fits, our analysis of the samples focused primarily on Mn(II) and Mn(IV) end-member samples with the lowest and highest AMOS determined by XANES Combo LCFs. Spectra of select Mn(II) (aqueous Mn^{2+}), Mn(III) (bixbyite, α-Mn_2O_3) and Mn(IV) (δ-MnO_2) reference materials and samples were typically fit by varying the interatomic distance (R), the coordination number (CN), the mean squared atomic displacement parameter (σ^2) and the change in threshold energy (ΔE_0). Since EXAFS fits are not able to distinguish between elements with similar scattering amplitudes (i.e., similar atomic numbers), we report the second-shell fit output for some samples as Mn-Me, where Me represents a metal with atomic number near or equal to that of Mn, which is most likely Fe given its abundance, if not Mn. The overall goodness-of-fit was assessed using the R-factor, which is the mean square difference between the fit and the data on a point-by-point basis: $R = \sum_i(data_i - fit_i)^2 / \sum_i(data_i)^2$. Additional details regarding the collection and analysis of XAS data are given in the SM.

3. Results

3.1 Dissolved Mn

Figure 2 compares the dMn and salinity in surface water of the four transects as a function of distance from the innermost fjord. For the AM transect, dMn and salinity exhibited distinct opposing trends with distance from inner- to outer-fjord. The highest dMn concentration of 80 nM was measured in surface water with the lowest salinity (4.0), which was located in the innermost fjord where meltwater discharge is high. The dMn concentration decreased with distance along the fjord, reaching a steady concentration in the range of 16-18 nM in higher salinity surface waters (salinity >23) over 35 km from the inner-fjord. These surface dMn levels are consistent with a recent study of dMn concentrations in the glacially-fed Copper River entering the Gulf of Alaska (Kandel and Aguilar-Islas, 2021) and are generally higher than the corresponding dFe levels (~7 - 35 nM in the outer fjord, maximum 230 nM nearest glacier discharge) at the same sample locations (van Genuchten et al., 2021). Particulate Mn was the dominant Mn form in the AM transect, with dMn levels representing 4-30% of total dissolvable Mn (TdMn; maximum TdMn >2000 nM), consistent with the high particle load shown by elevated turbidity. Similar to dMn, TdMn also decreased with increasing salinity and distance along the fjord (Figure S3). The decrease in TdMn with distance along the fjord matched the behaviour of turbidity, which was extremely high in the inner-fjord (600 NTU). Turbidity in the inner-fjord was characterized by a thin (< 1 m) near-surface layer of high turbidity that was visibly dissipated in the ship's wake (van Genuchten et al., 2021) and was not likely fully resolved by CTD data at 1 m resolution (i.e., the highest measured turbidity was likely an under-estimate).

Compared to the AM transect, the neighbouring GHF transect contained considerably lower dMn concentrations and the maximum dMn level was located mid-fjord rather than inner-fjord (Figure 1 and Figure S4). The dMn concentration in surface water at the inner-most GHF location was 22 nM (salinity of 12.7) and increased to 38 nM (salinity of 16.5) nearly 60 km from the inner-fjord. The same trend with distance was observed for dFe (5 – 12 nM) in this transect (van Genuchten et al., 2021) and reflects the outflow of a very large turbid lake (Lake Tasersuaq) mid-fjord, which likely contains elevated dMn and dFe signals compared to the freshwater sources (runoff and calved ice melt) in the inner-fjord (Hopwood et al., 2016). At distances further away from the inner-fjord (over 60 km from marine-terminating glacier Narsap Sermia), the dMn levels decreased as salinity increased, consistent with the AM transect. The lowest dMn concentration in the GHF transect of 9.5 nM was measured in the most saline surface water (27.8), which was >100 km from the inner-fjord. Similar to the AM transect, dMn in the GHF inner-fjord was a small fraction (~12-35%) of TdMn (Figure S3). While elevated turbidity occurs in the inner-fjord at sporadic depths close to the various glacier outflows, turbidity in GHF is much lower than AM, rarely exceeding 10 NTU in the main fjord and only exceeding 100 NTU within the shallow bay that receives Lake Tasersuaq outflow.

For the DI transect, a uniform decrease in dMn and increase in salinity with distance from inner- to outer-fjord was observed, consistent with the AM transect, but the dMn concentrations were higher along the DI transect (dFe levels ranged from 5 – 7 nM throughout the fjord (van Genuchten et al., 2021)). The inner-fjord surface waters with the lowest salinity (2.8) contained the highest dMn concentration of 135 nM, which exceeded peak dMn values of the AM (80 nM) and GHF (38 nM) transects. As distance along DI fjord progressed, dMn declined to 21 nM in the DI outer-fjord (salinity of 28.3) and dMn reached a minimum of 4.5 nM in the inner shelf (salinity of 33.8). Turbidity within DI was very similar to that observed in AM, characterised by a thin surface layer of high turbidity that spanned the inner-most 30 km of the fjord.

The dMn concentrations and salinity of the AF transect depended on location along the fjord, similar to the other transects. However, because of strong currents preventing sampling in the mid-fjord area of the AF transect, the dMn and salinity measurements are grouped in inner-fjord and outer-fjord clusters (dFe levels ranged from 4 – 6 nM throughout the fjord (van Genuchten et al., 2021)). The inner-fjord samples of the AF transect showed fairly stable and high dMn concentrations (128±8 nM) and low salinity (15.7±1.3). By contrast, the outer-fjord of the AF transect (Figure 2) was characterized by substantially lower dMn concentrations (20±7 nM) and higher salinities (31.5±0.9). Turbidity in AF was characterised by a distinct subsurface maximum around 10 m deep within the inner 30 km of the fjord and extremely high (>100 NTU) turbidity throughout the water column in the inner-most 10 km.

In all four fjords, dMn in surface waters appeared to behave relatively conservatively across the salinity gradient (linear regressions: R^2 GHF=0.59, AM=0.90, DI=0.99 and AF=0.97; Figure 2E, Figure S5), with GHF showing the most deviation from linearity due to the existence of 6 distinct major runoff outflows (3 marine-terminating glaciers: Kangiata Nunaata Sermia, Akullersuup Sermia, and Narsap Sermia; and runoff from 3 land-terminating glacier systems: Qamanaarsuup Sermia, Kangilinnguata Sermia and Saqqap Sermersua). Normalised to salinity, dMn concentrations were highest in AF and DI and lowest in GHF (Figure 2E). In all cases, the freshwater dMn endmember that can be estimated from regression of fjord data (range 49-233 nM) is similar to measured freshwater dMn concentrations in runoff from around south/west Greenland (range 27-234 nM) (Aciego et al., 2015; Hawkings et al., 2020).

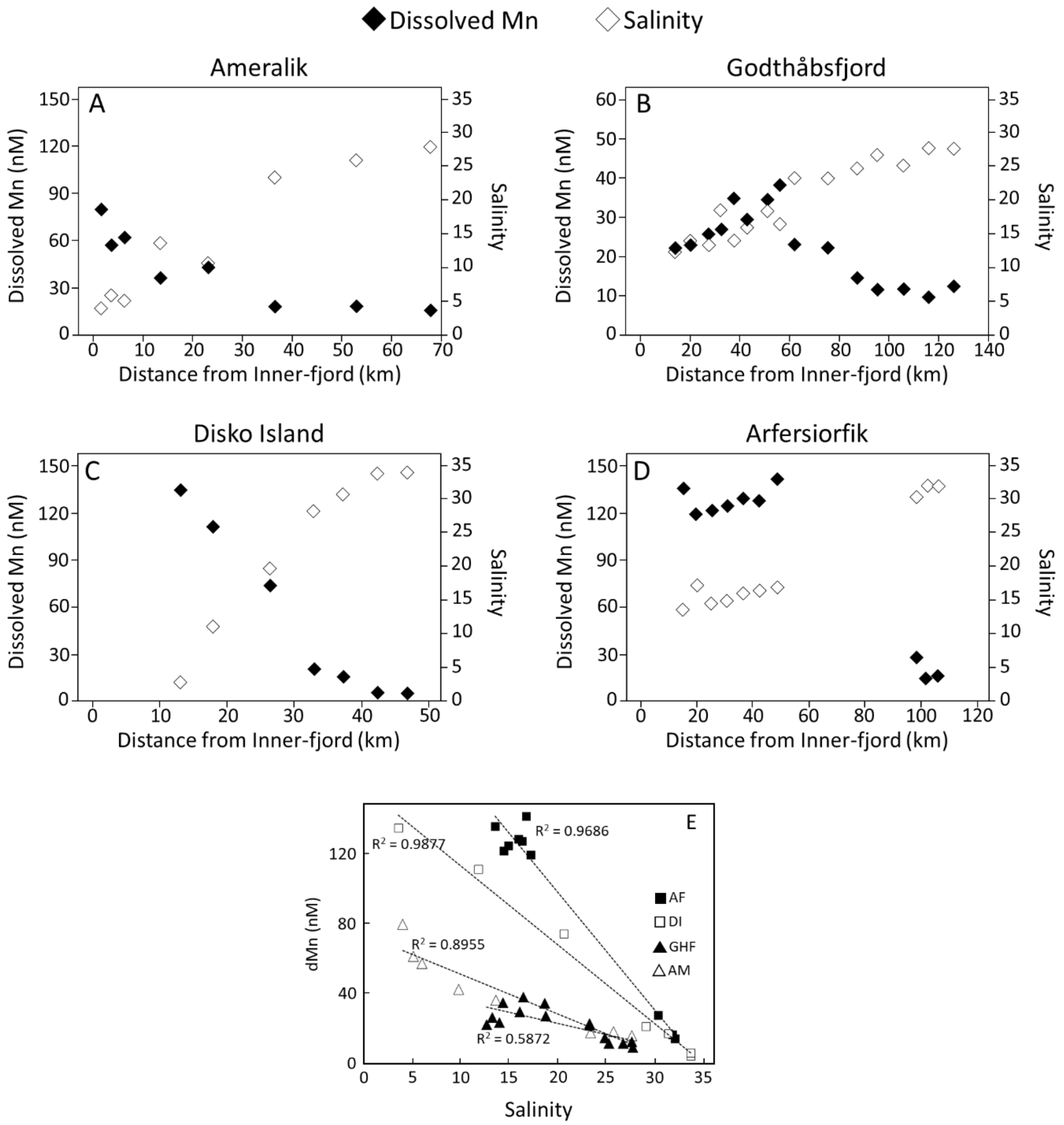

Figure 2. Dissolved Mn (dMn) and salinity along the Ameralik (AM; A), Godthåbsfjord (GHF; B), Disko Island (DI; C) and Arfersiorfik (AF; D) transects. Note that the y-axis for dMn in panel B (GHF) is different to the other panels. Salinity is defined according to the Practical Salinity Scale (Lewis and Perkin, 1978). Plots of dMn as a function of salinity and fits to linear regressions for each transect are shown in panel E.

3.2 Mn K-edge XANES spectroscopy

3.2.1 Ameralik and Godthåbsfjord transects

The XANES spectra of suspended particle samples from AM and GHF transects were all characterized by a small shoulder near 6547 eV and a double peak at 6552 and 6557 eV in the absorption maximum (Figure 3A). The small shoulder and first peak in the XANES spectra are consistent with the Mn(II) references ($MnSiO_3$ and Mn_2SiO_4) and the position of the second peak in the absorption maxima matches that of the Mn(III) reference (Mn_2O_3), suggesting the presence of multiple Mn oxidation states (Manceau et al., 2012). The XANES spectra of the AM and GHF samples largely matched the glacially-abraded rock flour spectrum (data overlay in Figure 3B), but none of the sample spectra were reproduced entirely by any of the 16 reference spectra given in Figure S2 (e.g., MnO, $MnCO_3$, $MnPO_4$, etc). While we do not report a Mn(II)-rich phyllosilicate reference spectrum here, the small shoulder and unique double peak in the XANES maximum of the samples closely resemble these features in the spectra of Mn(II)-bearing phyllosilicates (Lenz et al., 2014; Van Groeningen et al., 2020).

While the AM and GHF samples all displayed similar XANES fingerprints, some key differences are present, especially in the GHF depth profile samples. The overlain XANES spectra in Figure 3C show that the sample taken at 300 m has less amplitude in the shoulder and first absorption peak than the surface samples, but larger amplitude in the post-edge region at higher X-ray energy (arrow in Figure 3C), consistent with a greater fraction of oxidized Mn. Indeed, a higher fraction of Mn(III) in the GHF samples at depth is supported by the XANES Combo LCFs (Table 1). For example, the XANES LCFs of all AM samples yielded nearly identical average Mn oxidation states (AMOS) of 2.29–2.33, with similar contents of Mn(II) (67-71%) and Mn(III) (29-33%). The XANES LCFs of the GHF depth profile showed a steady increase in the AMOS of 2.31, 2.39, 2.41 and 2.57 for samples collected from the surface (glacier ice), 30 m, 200 m and 300 m depth. The XANES LCFs also indicated that the increase in

AMOS with depth was due exclusively to an increase in the Mn(III) content from 31 to 57% at the expense of Mn(II). The LCFs did not support the presence of Mn(IV) in any sample from the AM or GHF transects.

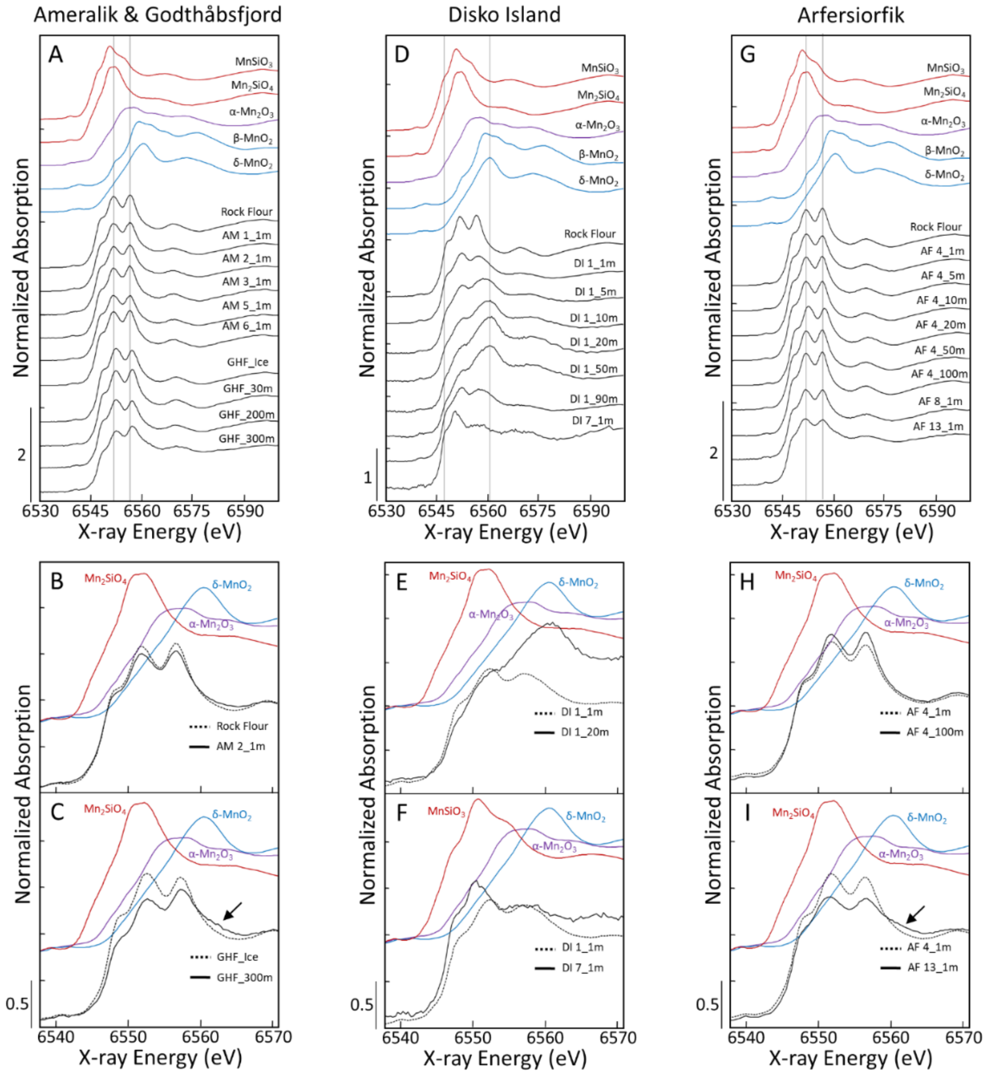

Figure 3. Mn K-edge XANES spectra of suspended particle samples (black lines) compared to the spectra of select Mn(II), Mn(III) and Mn(IV) references (in red, purple and blue, respectively). The left panels (A, B, C) show samples from Ameralik (AM) and Godthåbsfjord (GHF), the middle panels (D, E, F) show samples from Disko Island (DI) and the right panels (G, H, I) show samples from Arfersiorfik (AF). The vertical lines in panels A and G correspond to X-ray energies of 6552 and 6557 eV, whereas those in panel D correspond to 6547 and 6560 eV. Spectra in the upper panels (A, D, G) have been offset 0.5 A to facilitate comparison, whereas spectra in the lower panels are overlain to highlight key differences in XANES features. Sample names indicate location and depth (i.e. AF 4_100m represents the fourth station in the AF transect at 100 m depth).

3.2.2 Disko Island transect

The XANES spectra of Disko Island samples displayed large variation with location and depth, in contrast with the XANES spectra of the AM and GHF samples, indicating major changes in particulate Mn speciation over a similar spatial scale. The XANES spectrum of inner-fjord particles at 1 m depth exhibited the same features as the AM and Rock Flour samples (i.e. shoulder at 6547 eV, double-peaked absorption maximum), but these features in the DI sample were broadened and less distinct. The XANES spectra of the depth profile samples at this location showed a systematic shift in the absorption maximum to higher X-ray energy, consistent with an increase in Mn(IV) content (Figure 3E). For example, the XANES absorption maximum of samples collected from depths of 10 to 50 m was positioned at 6560 eV, which matches closely the position of the XANES absorption maximum of the Mn(IV) reference compound, δ-MnO_2 (a synthetic analogue of naturally-occurring birnessite (Zhu et al., 2012)). The XANES spectra of the depth profile samples also contained a post-edge oscillation with a local maximum near 6573 eV that is present in the post-edge region of the δ-MnO_2 reference spectrum. For the sample collected from the lowest depth (90 m), the XANES spectrum resembled that of the 1 m depth sample, suggesting a return to Mn(II)-dominated particles. The suspended particles collected from the outer-fjord at 1 m depth (Figure 3F) contained XANES features consistent with Mn(II), including the shoulder at 6547 eV and a dominant single peak in the absorption maximum at 6550 eV. However, this sample was a closer match to the reference spectrum of $MnSiO_3$ (pyroxmangite; a Mn(II)-bearing inosilicate (Manceau et al., 2012)), rather than a Mn(II)-rich phyllosilicate. This result indicates different Mn(II) host phases dominate in the inner- and outer-fjord regions of the DI transect, which could be due to preferential flocculation of phyllosilicates upon exposure to seawater leading to mineral differentiation along the particle plume.

Table 1: Summary of XANES LCFs by the Combo Method

Transect	Sample	Average Mn Oxidation State	%Mn(II)	%Mn(III)	%Mn(IV)	R-Factor
Ameralik and Godthåbsfjord	Rock Flour	2.29 ± 0.08	71	29	0	0.0149
	AM 1_1m	2.31 ± 0.08	69	31	0	0.0101
	AM 2_1m	2.33 ± 0.08	67	33	0	0.0093
	AM 3_1m	2.32 ± 0.08	68	32	0	0.0129
	AM 5_1m	2.29 ± 0.08	71	29	0	0.0098
	AM 6_1m	2.29 ± 0.08	71	29	0	0.0085
	GHF Ice	2.31 ± 0.08	69	31	0	0.0147
	GHF_30m	2.39 ± 0.08	61	39	0	0.0201
	GHF_200m	2.41 ± 0.08	59	41	0	0.0129
	GHF_300m	2.57 ± 0.08	43	57	0	0.0063
Disko Island	DI 1_1m	2.40 ± 0.08	61	38	1	0.0024
	DI 1_5m	2.76 ± 0.08	42	40	18	0.0039
	DI 1_10m	3.05 ± 0.04	28	38	33	0.0057
	DI 1_20m	3.27 ± 0.04	15	42	42	0.0141
	DI 1_50m	3.21 ± 0.04	18	44	39	0.0117
	DI 1_90m	2.47 ± 0.08	57	39	4	0.0025
	DI 7_1m	2.28 ± 0.08	72	28	0	0.0085
Arfersiorfik	AF 4_1m	2.26 ± 0.08	74	26	0	0.0121
	AF 4_5m	2.27 ± 0.08	73	27	0	0.0146
	AF 4_10m	2.27 ± 0.08	73	27	0	0.0148
	AF 4_20m	2.27 ± 0.08	73	27	0	0.0132
	AF 4_50m	2.28 ± 0.08	72	28	0	0.0155
	AF 4_100m	2.25 ± 0.08	75	25	0	0.0172
	AF 8_1m	2.25 ± 0.08	75	25	0	0.0239
	AF 13_1m	2.33 ± 0.08	67	33	0	0.0104

The errors in the average Mn oxidation state represent estimated uncertainty of the Combo method. The origin of uncertainty in XANES Combo LCFs is described in detail in Manceau et al. (2012).

The XANES Combo LCFs confirmed the transition from Mn(II)-rich to Mn(IV)-rich particles with depth for the DI transect, with a maximum Mn(IV) content detected at 20 m (Table 1). The AMOS of particles collected at 1 m was determined to be 2.40 and consisted primarily of

Mn(II) (61%), with a lower fraction of Mn(III) (38%). The LCFs indicated an almost linear increase in AMOS with depth to 20 m at this location, with AMOS values of 2.76, 3.05 and 3.27 detected for samples at 5, 10 and 20 m depth. This change in AMOS was mainly due to an increase in Mn(IV) from 18% to 42% at the expense of Mn(II). The LCF-derived Mn(III) content for all samples in the depth profile was essentially constant, varying from 38 to 44% (Table 1). As depth increased beyond 20 m, the AMOS of suspended particles decreased, with the LCFs indicating the largest AMOS decline at depths of 50 m (AMOS of 3.21) to 90 m (AMOS of 2.47). Finally, the XANES LCFs of the sample collected from the DI outer-fjord indicated the predominance Mn(II) (AMOS of 2.28; 72% Mn(II), 28% Mn(III)), which is consistent with the inner-fjord sample at 1 m, despite their different XANES features (Figure 3F).

3.2.3 Arfersiorfik transect

Similar to the AM transect samples, all AF suspended particles exhibited similar XANES spectra, suggesting no major structural modifications with location or depth. The XANES spectra of each AF sample contained the same characteristic shoulder at 6547 eV and double peaks at 6552 and 6557 eV as was observed for the AM and GHF samples. In contrast to the moderate differences in XANES spectra of the GHF depth profile samples, particles from the AF transect depth profile did not display significant changes in the XANES spectra (Figure 3H). However, we note that the depth profile (100 m) of AF transect was not as deep as that of GHF (300 m) due to the shallower nature of the inner-fjord. While all samples in the AF transect exhibited similar XANES spectra, some deviation in XANES features were present for the samples collected at 1 m depth in the inner- and outer-fjord regions. The AF 13 sample, which was collected approximately 100 km downstream of the AF 4 sample (Figure 1C), contained higher amplitude in the XANES region indicative of oxidized Mn (arrow in Figure 3I).

The XANES Combo LCFs confirmed the predominance of Mn(II) in the AF transect samples. A relatively narrow range of AMOS from 2.26-2.33 was detected for all AF transect samples (all samples were within the estimated uncertainty of ±0.08), with the Mn(II) content varying from 67-74% and the Mn(III) content varying from 26-33%. The LCFs detected no Mn(IV) for any sample, consistent with the AM and GHF transects.

3.3 Mn K-edge EXAFS spectroscopy

Principal component analysis of the EXAFS dataset (>20 samples) revealed a minimum in the indicator function (IND) with only two independent components (Figure S6). Therefore, the major variance in the EXAFS spectra of all samples collected across the four transects can be reproduced with only two end-member spectra. Characteristic features of the XANES and EXAFS spectra indicate that the end-members include Mn(II)-rich and Mn(IV)-rich particles. The EXAFS spectra of these two distinct groupings are analysed together in the following subsections.

3.3.1 Mn(II)-rich end-member samples

The EXAFS spectra of the Mn(II)-rich samples all displayed similar features in the major EXAFS oscillations, including a split first peak from 2.8 to 4.6 Å^{-1}, a relatively small feature near 5.2 Å^{-1} and an intense peak near 5.9 Å^{-1}. While all Mn(II)-rich sample spectra contained the same EXAFS fingerprints, no single reference compound could reproduce these features (Figure S7), which was also the case for the corresponding XANES spectra. We note that the Mn(II)-rich outer-fjord sample for the DI transect, which had a different XANES spectrum from the samples given in Figure 3, could not be further analysed for EXAFS here because of an insufficient signal-to-noise ratio. The Fourier-transformed EXAFS spectra of the Mn(II)-rich samples were characterized by two major peaks: a high and low amplitude peak positioned at short and long R-values, respectively. The position and amplitude of the large peak was a close match to that of the aqueous Mn(II) reference spectrum, whereas the lower amplitude peak at longer R did not match the references. To quantitatively determine the Mn coordination environment in these samples, shell-by-shell fits of these peaks were performed.

The first shell of all Mn(II)-rich samples was fit with an Mn-O path at 2.16-2.17 Å, which is a good match to the fit-derived $R_{Mn\text{-}O}$ value (2.18 Å) for aqueous Mn(II) (Table 2). The slightly shorter $R_{Mn\text{-}O}$ of the samples compared to the aqueous Mn(II) reference is attributed to the presence of Mn(III), which has a shorter $R_{Mn\text{-}O}$ (Table 2). The fit of the second-shell peak of the Mn(II)-rich samples was more complicated because of the possibility of a variety of atomic pairs, such as Mn-Me, Mn-Al and Mn-Si, depending on the Mn host phase. Despite the potential for different atomic pairs, the best fit of all Mn(II) end-member samples was achieved with a single Mn-Me atomic pair at 3.15 Å, which is consistent with Mn-Me bonds from edge-sharing $Mn^{II}O_6$ and MeO_6 octahedra (Wyckoff, 1963). Many separate attempts to fit an Mn-Al or Mn-Si path in lieu of, or in addition to, the Mn-Me path were not successful, yielding non-physical (negative) CN values. A Mn-Me path at 3.3-3.4 Å was also attempted in the fit, but it was not supported (negative CN values or convergence to 3.15 Å). The fit-derived $CN_{Mn\text{-}Me}$ varied slightly across all samples (1.0 – 1.8), with the Rock Flour sample having a larger CN (1.8) than the fjord samples (1.0 – 1.2).

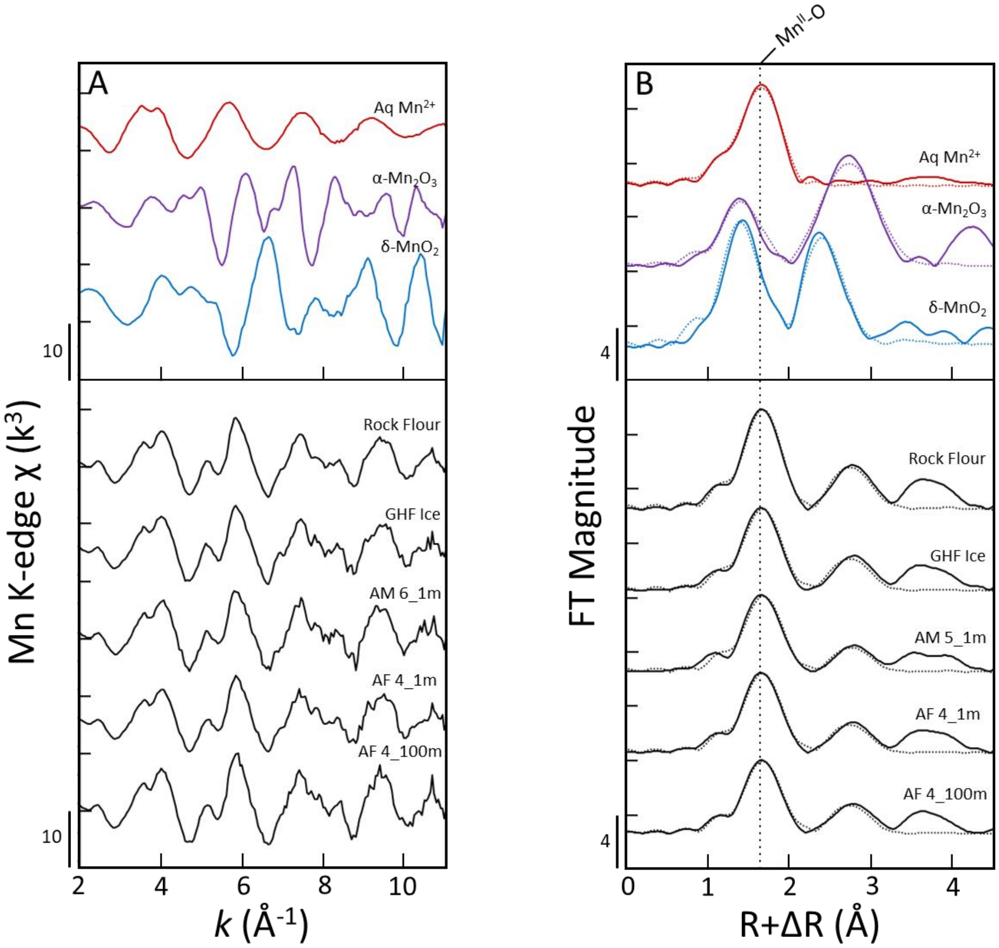

Figure 4: Mn K-edge EXAFS spectra and corresponding Fourier transforms of Mn(II)-bearing end-member suspended particle samples compared to select reference materials. The fitting output (dotted lines) is overlain to the data (solid lines) in panel B.

Table 2: Summary of Shell Fits of Mn-bearing References and Suspended Particles

	Name	Atomic Pairs	CN	R (Å)	σ^2 (Å^2)	ΔE_0 (eV)	R-Factor
Reference Materials	Aq Mn^{2+}	Mn-O	7.1 (0.6)	2.18 (0.01)	0.010 (0.001)	-10.0 (1.0)	0.012
	α-Mn_2O_3	Mn-O	2.6 (1.0)	1.92 (0.03)	0.004 (0.004)	-17.8 (5.2)	0.020
		Mn-Mn1	5.3 (4.0)	3.09 (0.04)	0.009 (0.007)		
		Mn-Mn2	4.0 (3.2)	3.52 (0.05)	σ^2_{Mn-Mn1}		
	δ-MnO_2	Mn-O	4.7 (0.7)	1.89 (0.01)	0.004 (0.001)	-20.1 (1.5)	0.011
		Mn-Mn	4.1 (0.9)	2.88 (0.02)	0.007 (0.002)		
Mn(II) End-member Samples	Rock Flour	Mn-O	4.8 (0.7)	2.16 (0.01)	0.005 (0.002)	-7.9 (1.6)	0.028
		Mn-Me	1.8 (0.3)	3.15 (0.02)	0.007		
	GHF Ice	Mn-O	4.2 (0.7)	2.16 (0.01)	0.006 (0.002)	-7.9 (1.9)	0.038
		Mn-Me	1.4 (0.3)	3.15 (0.02)	0.007		
	AM 5_1m	Mn-O	3.7 (0.7)	2.17 (0.01)	0.005 (0.002)	-7.3 (2.0)	0.044
		Mn-Me	1.0 (0.3)	3.15 (0.02)	0.007		
	AF 4_1m	Mn-O	3.8 (0.6)	2.16 (0.01)	0.005 (0.002)	-8.1 (1.7)	0.030
		Mn-Me	1.2 (0.3)	3.15 (0.02)	0.007		
	AF 4_100m	Mn-O	3.3 (0.5)	2.16 (0.01)	0.005 (0.002)	-8.2 (1.7)	0.031
		Mn-Me	1.2 (0.2)	3.15 (0.02)	0.007		
Mn(IV) End-member Samples	DI 1_10m	Mn-O1	1.5 (0.5)	1.89 (0.01)	0.005 (0.003)	-10.0 (2.3)	0.025
		Mn-O2	0.7 (0.3)	2.18 (0.03)	0.005		
		Mn-Me	1.0 (0.1)	2.86 (0.02)	0.007		
	DI 1_20m	Mn-O1	1.3 (0.6)	1.90 (0.02)	0.005 (0.004)	-17.2 (2.8)	0.031
		Mn-O2	0.6 (0.4)	2.21 (0.03)	0.005		
		Mn-Me	0.9 (0.1)	2.87 (0.02)	0.007		
	DI 1_50m	Mn-O1	1.2 (0.5)	1.89 (0.01)	0.004 (0.004)	-19.3 (2.6)	0.025
		Mn-O2	0.5 (0.4)	2.19 (0.03)	0.005		
		Mn-Me	0.9 (0.1)	2.85 (0.02)	0.007		

CN represents the coordination number, R the interatomic distance, σ^2 the mean squared atomic displacement and ΔE_0 represents the change in threshold energy. The passive electron reduction factor, S_0^2, was fixed at 0.7. Fitting parameters allowed to float are accompanied by fit-determined standard errors in parenthesis, while constrained parameters appear without a parenthesis. All fits were carried out from 1 to 3.5 Å in R+ΔR-space. The number of independent points (N_{IDP}) in the fits was 12.6 and the number of variables (N_{Var}) was 4 to 9.

3.3.2 Mn(IV)-rich end-member samples

The Mn(IV)-rich sample spectra all displayed characteristic features in the major EXAFS oscillations that were also present in the δ-MnO_2 reference spectrum, including the distinct staircase from 4 to 6 $Å^{-1}$, which is indicative of nanoscale MnO_2 (Grangeon et al., 2010; Ling et al., 2018), and the large peak from 6 to 7 $Å^{-1}$ (grey bars in Figure 5A; Figure S7). The similarity between the EXAFS spectra of the Mn(IV)-rich samples and nanocrystalline δ-MnO_2 is consistent with their comparable XANES spectra. The Fourier-transformed EXAFS spectra further confirm that the average Mn coordination environment in the Mn(IV)-rich samples matches that of δ-MnO_2. For example, the samples and δ-MnO_2 all displayed two main peaks of similar relative amplitude positioned at nearly identical R-values (vertical lines in Figure 5B). However, the first-shell peak of the samples also contained a visible shoulder at higher R, consistent with the presence of Mn(II).

Fits of the major component of the first-shell peak for the Mn(IV)-rich samples returned similar $R_{Mn\text{-}O}$ values for all samples (1.89-1.90 Å), which was identical within fit-derived uncertainties to the $R_{Mn\text{-}O}$ for δ-MnO_2 (1.89 Å, Table 2). Despite the relatively low Mn(II) content in these samples (15-28%), a second Mn-O peak at longer R (2.18-2.21 Å) was resolved in the first-shell peak using a constrained σ^2 equal to that of the Mn(II)-rich samples (0.005 $Å^2$). The $R_{Mn\text{-}O}$ of this second Mn-O atomic pair is comparable to that of the aqueous Mn(II) reference spectrum (2.18 Å, Table 2), but the exact host phase for Mn(II) in the Mn(IV)-rich samples could not be identified further. The second-shell peak of all Mn(IV)-rich samples was fit with an Mn-Me path at 2.85-2.87 Å, which closely reproduced the analogous Mn-Mn path in the fit of δ-MnO_2 (2.88 Å). In contrast to the fits of the Mn(II)-rich samples, which yielded slight differences in $CN_{Mn\text{-}Me}$, the second-shell fits of the Mn(IV) samples yielded similar CNs for all samples (Table 2). Although the shape of the EXAFS spectra and the fit-derived $R_{Mn\text{-}O}$ and $R_{Mn\text{-}Me}$ values for the Mn(IV)-rich samples matched δ-MnO_2, the fit-derived CNs for the samples were lower than the values expected based on the crystal structure of birnessite (Lanson et al., 2002). This result can be explained by destructive interference of multiple EXAFS oscillations causing a decrease in amplitude of the EXAFS data and Fourier transforms, which has been reported previously for birnessite and δ-MnO_2 when Mn(II,III) is present in the solid phase, consistent with our samples (Webb et al., 2005).

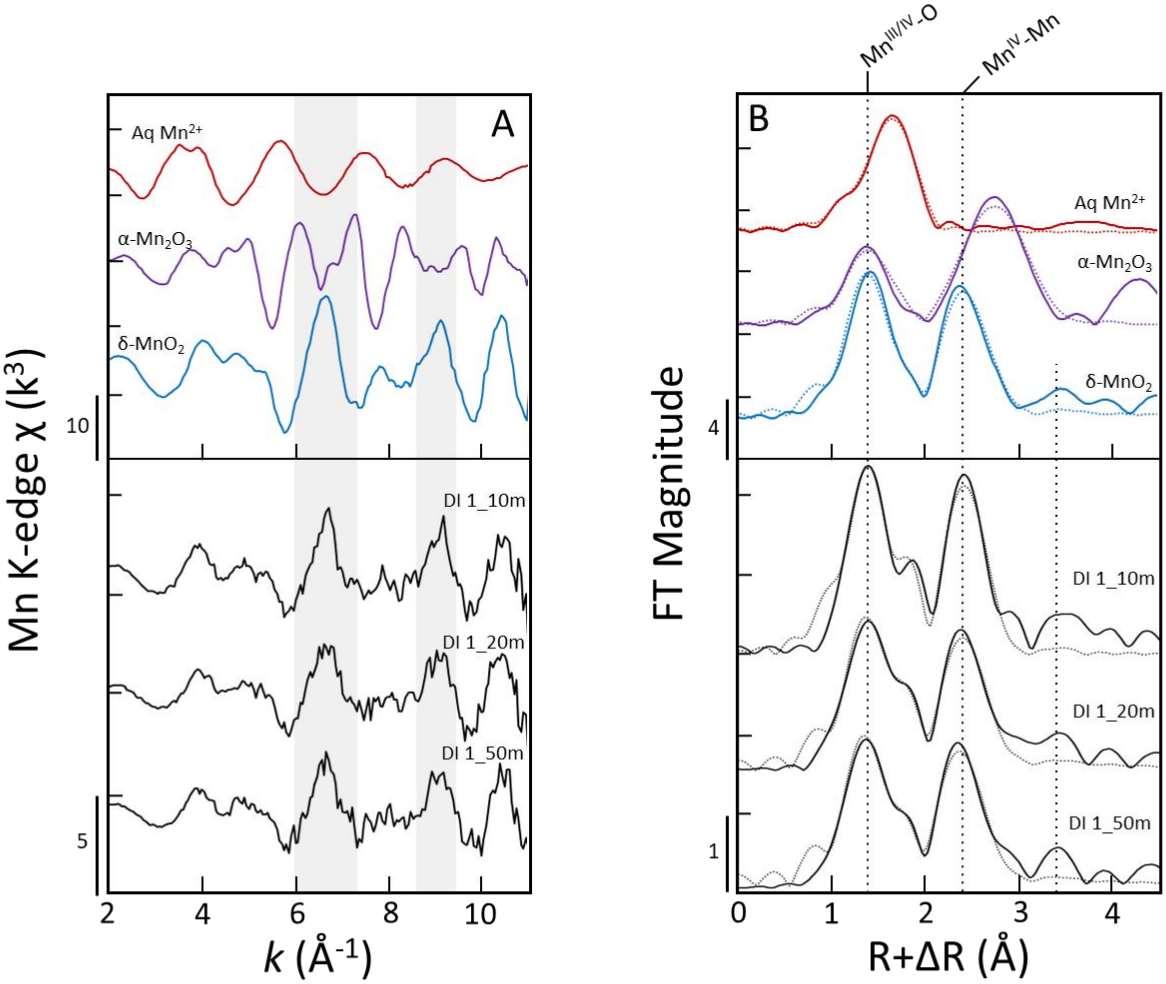

Figure 5: Mn K-edge EXAFS spectra and corresponding Fourier transforms of Mn(IV)-bearing end-member suspended particle samples compared to select reference spectra. The fitting output (dotted lines) is overlain to the data (solid lines) in panel B. The grey vertical bars (6 – 7.3 $Å^{-1}$, 8.6 – 9.2 $Å^{-1}$) highlight key features in the EXAFS spectra of the Mn(IV)-rich samples.

4. Discussion

4.1 Identity of the Mn(II)- and Mn(IV)-rich host phases

Before discussing the behaviour of dMn, we will first identify the host phases of Mn(II) and Mn(IV) in the suspended particles to aid our interpretation of dMn trends. The Mn(II)-bearing suspended particles were widespread, having been collected from all four transects across a range of environments, including fjord surfaces, depth profiles and calved glacier ice. The EXAFS analysis indicated that the second-shell peak of the Mn(II) end-member samples was best fit with a Mn-Me path at 3.15 Å. This $R_{Mn\text{-}Me}$ is consistent with Mn-Me bonds from edge-sharing octahedra, but an Mn-Me bond with this length is not unique to any single Mn(II)-bearing mineral. In particular, rhodonite ($MnSiO_3$), tephroite (Mn_2SiO_4) and manganosite (MnO) all contain at least some Mn-Me bonds near 3.15 Å (Wyckoff, 1963; Yamazaki and Toraya, 1999; Nelson and Griffen, 2005). However, the presence of a significant fraction of these minerals can be ruled out because the major second-shell atomic pair in rhodonite and tephroite is Mn-Si, which was not detected by the fit, and the manganosite XANES (Figure S2) and EXAFS spectra (Figures EA6) contained characteristic features that were not present in the sample spectra. Rather than these three minerals, Mn(II)-bearing phyllosilicates, such as biotite or chlorite, are the likely Mn(II) host phases. For example, if Mn(II) occupied a cation site in the brucite-like sheet of phyllosilicates, the dominant atomic pair in the second Mn coordination sphere would be a 6-fold coordinated cation, consistent with the fit-derived $R_{Mn\text{-}Me}$ of 3.15 Å. Furthermore, the XANES spectra of the samples closely resembled that of Mn(II)-rich phyllosilicates reported previously (Lenz et al., 2014; Van Groeningen et al., 2020). The widespread presence of Mn(II)-bearing phyllosilicates is also supported by our previous work in the same fjords, which showed that Fe(II) was hosted by phyllosilicates in the majority of suspended particle samples (van Genuchten et al., 2021).

For the Mn(IV)-rich end member samples, which were collected primarily from the DI depth profile between 10 and 50 m, the XANES and EXAFS spectra matched those of the δ-MnO_2 reference mineral. The shell-by-shell fits of the Mn(IV)-rich samples ($R_{Mn\text{-}O}$ = 1.89-1.90 Å, $R_{Mn\text{-}Me}$ = 2.85-2.87 Å) also matched the fitting output of δ-MnO_2 (Table 2) and are consistent with edge-sharing Mn(IV) octahedra (Lanson et al., 2002). Therefore, we conclude that the Mn(IV)-rich particles consist of nanoscale birnessite-like MnO_2. Other types of MnO_2, including crystalline pyrolusite (β-MnO_2), can be excluded based on key differences in the XANES (Figure S2) and EXAFS spectra (Figure S7). While the EXAFS analysis indicated the presence nanoscale MnO_2 akin to birnessite, a considerable fraction of reduced Mn(II,III) was also detected (Table 1). Previous work has shown that synthetic and naturally-occurring birnessites can contain high Mn(III) content (>40%), leading to AMOS values much lower than 4.0 (Toner et al., 2005; Ling et al., 2018). The presence of reduced Mn is particularly relevant for biogenic birnessites, the most common form of MnO_2 in nature (Tebo et al., 2004), which also often contain >10% Mn(II), depending on reaction conditions (e.g. time, solution composition, type of Mn(II)-oxidizing microorganisms) (Webb et al., 2005; Yu et al., 2012). As a consequence, the maximum XANES-derived Mn(IV) content of 42% in the DI depth profile does not necessarily translate to 42% of solid-phase Mn speciated as birnessite. Rather, birnessite-like Mn is expected to be the dominant Mn phase in the Mn(IV)-rich samples (i.e., >70-80% of total particulate Mn assuming birnessite is composed of 50-60% Mn(IV)) because a fraction of the lower valent Mn detected by XANES LCFs is likely part of the birnessite mineral structure.

4.2 Behaviour of dMn

Measurements of dMn for all fjords showed a similar inverse relationship in dMn concentration with salinity and distance along the fjord. For example, the maximum dMn levels for the AM (80 nM), DI (135 nM) and AF (130 nM) transects were all inner-fjord. The exception was the GHF transect, which showed a maximum dMn (38 nM) mid-fjord likely due to the input of the turbid Lake Tasersuaq outflow with locally higher dMn concentrations than are associated with freshwater inputs at the inner-fjord. Although dMn data elsewhere around Greenland in near-shore waters are limited (Colombo et al., 2020; Krisch et al., 2021), these dMn values are consistent with glacially-fed outflows of the Copper River to the Gulf of Alaska (Kandel and Aguilar-Islas, 2021) and other reported freshwater concentrations (24-234 nM) (Aciego et al., 2015; Hawkings et al., 2020), which is reasonable considering the relative salinities. The general decrease in dMn with salinity could be explained by a combination of dMn oxidation and precipitation, dilution and likely some degree of biological drawdown. Considering the low primary production associated with high turbidity surface waters in inner-fjord environments, corresponding approximately to salinities of ~15 or less herein, inorganic processes (oxidation and precipitation) likely account for the majority of any non-conservative mixing. Yet the similar linear gradient of surface water dMn levels against salinity across 4 diverse fjords suggests dilution was the main process affecting dMn concentrations in surface waters and that dMn dynamics are largely conservative on this spatial scale. The overlapping range of measured freshwater concentrations in West Greenland (27-234 nM) (Aciego et al., 2015; Hawkings et al., 2020), and freshwater endmembers derived from regression of fjord data (49-233 nM) also suggests that dMn sources other than freshwater derived dMn are likely minor. If other dMn sources to the outflowing surface layer on the same spatial/temporal scale were large by comparison, such as entrainment of a net benthic efflux of dMn from shallow sediments (Wehrmann et al., 2014), dMn concentrations at zero salinity derived from regression would be larger than measured freshwater concentrations, and dMn would be less conservative across the salinity gradient.

While a decrease in concentration with increasing salinity has also been noted for dFe in these fjords (van Genuchten et al., 2021), the behaviour of dMn and dFe is not identical, which was also observed recently in the Copper River particle plume (Kandel and Aguilar-Islas, 2021). This is immediately apparent when comparing the strong linearity in dMn concentrations across the salinity gradient (Figure S5), with the non-linear loss of dFe along the same transects (van Genuchten et al., 2021). One way to visualise the corresponding behaviour of these two trace metals is to compare the dMn/dFe ratio as a function of salinity. In Figure 6, we combine the current dMn dataset with dFe measurements from the same samples reported previously and determine the dMn/dFe ratio of our samples alongside other dMn/dFe ratios reported around Greenland (Aciego et al., 2015; Hawkings et al., 2020; Achterberg et al., 2021; Krisch et al., 2021). In general, the dMn/dFe ratio exhibits several key features with salinity (and distance along the fjord). For low salinity inner-fjord environments close to meltwater outflows, the dMn/dFe ratio is variable but generally low because the dFe content in meltwater is, on average, much higher than dMn (Aciego et al., 2015; Hawkings et al., 2020). This is expected based on the crustal abundances of Fe (~5%) and Mn (~0.1%) and the lithogenic source of most metals in runoff (Hartmann et al., 2012). As salinity increases to intermediate values (10-20), the dMn/dFe ratio uniformly exceeds 2 and is often above 10 (mean of 15±12). This trend arises from the lower stability of dFe across the salinity gradient (Boyle et al., 1977) and higher likelihood of dFe precipitation than dMn, particularly in surface waters (Sunda et al., 1983) due to low concentrations of organic ligands that are required to stabilize dFe at nanomolar concentrations in saline waters (Ardiningsih et al., 2020). Finally, at the highest salinities, the dMn/dFe ratio decreases again because dMn(II) is oxidized and ultimately precipitates, whereas the remaining dFe concentration depends to a greater extent on complexation and stabilization by organic ligands (Gledhill and Buck, 2012; Ardiningsih et al., 2020; Achterberg et al., 2021). Although we did not perform dMn speciation measurements, we do not expect a large fraction of strong aqueous Mn-ligand complexes near the inner-fjord where the dMn level peaked because existing work suggests the complexation of Fe in similar environments is characterised by a pool of ligands which are weaker than their marine counterparts (Ardiningsih et al., 2020).

Comparing data across fjords did not reveal any clear relationships between dMn concentration and particulate Mn speciation or underlying bedrock geology. For example, dMn concentrations in the inner-fjord of the GHF transect were lower than those of the AM and AF transects, but all three fjords were dominated by Mn(II)-bearing suspended particles derived from the same Precambrian shield geology. While precise fjord-scale freshwater budgets are not available, a critical difference between GHF and the other fjords studied is that a significant fraction of freshwater entering GHF is from the melting of calved ice (i.e. icebergs) within the fjord. For the time period 2002-2012, liquid runoff into the fjord is estimated as 18.4 ± 5.8 Gt yr^{-1} from the ice sheet and 7.5 ± 2.1 Gt yr^{-1} from other runoff (Langen et al., 2015). An estimate of ice calving for a similar time period is 7.6 ± 1.5 km^3 (Mortensen et al., 2011) with 70% of calved ice melting mainly within the inner fjord. It can therefore be approximated that ~20% of the freshwater entering GHF is from calved ice melting. As elevated trace metal concentrations in runoff primarily arise from sedimentary interaction, the concentrations of dissolved trace metals in calved ice are generally expected to be lower than runoff. Regional differences depending on the residence time of freshwater in subglacial and proglacial environments are also likely. While we cannot comment on the underlying cause herein, the highest dMn concentrations normalized to salinity herein in the Arfersiorfik region also correspond to an area with the highest reported dNi and dCo concentrations reported to date in coastal waters around Greenland (25-29 nM dNi and 6-7 nM dCo, (Krause et al., 2021)). Dissolved Mn data for calved ice are sparse, but the limited available dFe data do support the hypothesis of changes in the freshwater concentrations contrasting proglacial runoff with freshly melted ice (reported means for West Greenlandic runoff range 53 nM-3.7 µM, the range for West Greenlandic ice is <3-300 nM) (Statham et al., 2008; Bhatia et al., 2013; Hopwood et al., 2016; Stevenson et al., 2017; Hawkings et al., 2020). Differences in the origin of freshwater (tundra runoff, snow melt, glacier runoff and calved ice melting) likely therefore contribute to the different mean freshwater endmembers for these fjord systems.

The DI and AF transects in the Disko Bay region contained similar maximum dMn levels, but the suspended particle speciation in these fjords varied (i.e., birnessite-like Mn(IV) derived from tertiary basalts in DI, Mn(II)-bearing solids in AF). These inter-fjord comparisons suggest a decoupling between particulate and dissolved Mn, which is inconsistent with the notion that increased dMn levels are generally favoured in the presence of Mn(II)-bearing minerals because of their higher solubility than Mn(IV)-bearing solids (Ball and Nordstrom, 1991). The decoupling of aqueous and particulate Mn is consistent with a similar decoupling of dissolved and solid-phase Fe in these fjords (i.e. changes in Fe mineralogy did not correlate with changes in dFe (van Genuchten et al., 2021)) and suggests that dMn concentrations on the scales of the fjord are regulated by processes other than particulate Mn solubility. This does not preclude a role of particle dissolution in driving elevated freshwater dMn concentrations, but suggests that limited further net-dissolution occurs on the timescale during which saline waters circulate through glacier fjord systems. This contrasts with process studies concerning Fe and Mn dissolution from aerosol particles, where dMn release at low nanomolar concentrations scales linearly with particulate Mn availability and Fe release is less linear (Mendez et al., 2010). A critical difference between dust addition into the offshore ocean and runoff-derived particle addition to the coastal ocean is particle loading. Runoff around Greenland is estimated to have an average particle load of ~1 g/L, with a few notable catchments including AM estimated to be 2-3 times higher than average (Overeem et al., 2017). The resulting high particle loads and surface area close to glacier outflows may promote scavenging and reduce light, both of which may disfavour dMn stability and promote Mn(II) oxidation, consistent with the low dMn/dFe ratio at low salinities (Figure 6). Similar dynamics likely influence the upstream dMn concentrations in the corresponding freshwater environments.

Although our dataset suggests that dMn and particulate Mn speciation are decoupled in these transects, it is important to acknowledge several caveats to this conclusion. First, multiple sampling campaigns were required to obtain the entire dataset, which prevented the collection of all data within a short time frame. However, all data were collected in the summer months close to the peak of the meltwater season. Even with data collected in different seasons, there is still not much evidence of pronounced trace metal concentration changes throughout the year based on the limited available data. For example, Godthåbsfjord dFe concentrations more than ~50 km away from the glacier termini almost all fall within the 4-10 nM range during the months May, August and September covering conditions of very low, peak and post-peak runoff (Hopwood et al., 2016; van Genuchten et al., 2021; Krause et al., 2021). Therefore, the collection of data in multiple sampling campaigns is not expected to impact our conclusions. The second caveat is related to limited access to beam lines for synchrotron work and the several hours required for XAS data collection per sample. While our particle dataset is large, it was not logistically feasible to conduct high resolution surveys with multiple profiles in multiple fjords. We therefore opted to conduct profiles and transects to select for areas with notable gradients where the largest changes in speciation would be plausibly expected to occur. There is thereby a bias towards lateral transects because, as documented by turbidity in full depth profiles of these fjords (van Genuchten et al., 2021), the vast majority of the particles advected away from the glaciers studied herein are in a thin surface-only layer. Considering the two-dimensional estuarine circulation typical of large Greenlandic fjords in summer, near-surface plumes are also the most relevant with respect to down-fjord advection of particles (Mortensen et al., 2014; Straneo and Cenedese, 2015).

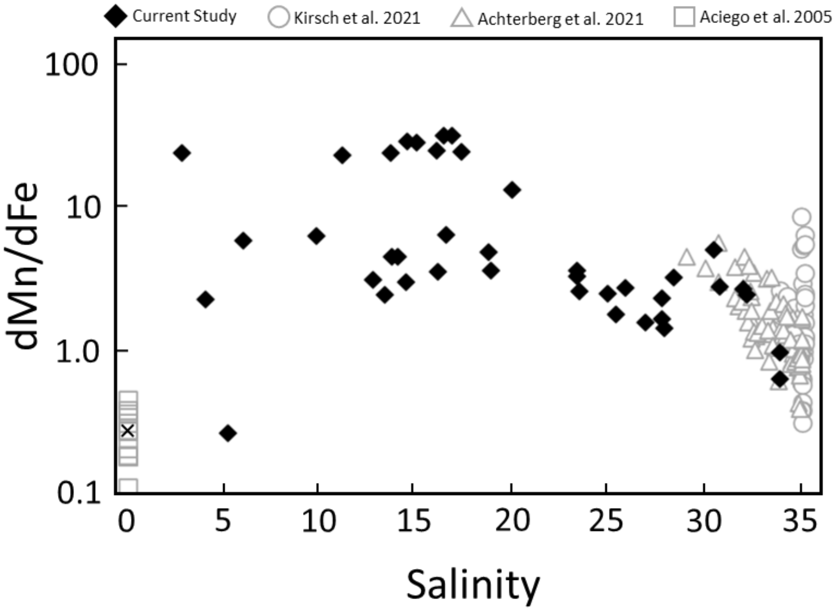

Figure 6. Ratio of dMn/dFe as a function of salinity for the fjords in the current study (filled diamonds) compared to data obtained from the scientific literature (open symbols). The squares, circles and triangles represent data reported from W Greenland (Aciego et al., 2015), NE Greenland (Krisch et al., 2021) and E Greenland respectively (Achterberg et al., 2021). The X symbol represents the average dMn/dFe ratio reported from Leverett Glacier, W Greenland (Hawkings et al., 2020). The data presented above were all collected in early to late summer. A plot of dMn/dFe ratios using only the data in this study is given in Figure S8.

4.3 Changes in particulate Mn speciation with depth

One of the most distinct trends revealed by the Mn K-edge XAS data was the change in particulate Mn speciation with depth in DI fjord. Although the AMOS was found to increase slightly in the GHF depth profile (increase from 2.3 to 2.6 over 300 m depth), the change in AMOS was most pronounced in the DI depth profile in the inner-fjord. The DI depth profile also had the unique feature that the AMOS of particles increased from 2.4 near the surface to a maximum near 3.3 at 20 m depth, then decreased again to 2.5 at 90 m depth. These observations could be explained by several scenarios. The first is simply that particulate Mn at depth has a different origin that is enriched in Mn(IV) than the Mn(II)-rich surface particles. This scenario is consistent with lateral transport of particulate Mn(IV) that could occur from a source such as submarine groundwater discharge, though dMn can also be easily transported laterally and oxidized subsequently (Jensen et al., 2020; Xiang and Lam, 2020). Subsurface currents that erode the walls of the fjord could also contribute to different materials found at depth. The second scenario is that glacial meltwater entering DI fjord initially contained MnO_2 that was photoreduced near the fjord surface, but was preserved or re-oxidized in particles rapidly sinking below the photic zone. This interpretation is based on the well-documented instability of MnO_2 in the presence of light (Matsunaga et al., 1995; Marafatto et al., 2015; Zhang et al., 2018) and the common observation of increased surface water dMn concentrations relative to deeper seawater (Sunda, 2012; Noble et al., 2013), although we note dMn depth profiles near coasts can be altered by subsurface dMn inputs. The presence of meltwater-derived Mn(IV) in DI fjord and not the other fjords is also consistent with our previous work showing distinct Fe mineralogy of DI fjord particles (oxidized Fe(III) (oxyhydr)oxides) compared to AM and AF particles (Fe(II)-

rich phyllosilicates), which can be attributed to differences in fjord bedrock geology (Dawes, 2009; van Genuchten et al., 2021). However, some weaknesses of this photoreduction scenario are that MnO_2 photoreduction is expected to lead to different particulate Mn species (e.g., rhodochrosite) than the Mn(II)-bearing phyllosilicates collected from the top of the DI depth profile and photoreduction alone cannot explain why the sample at the lowest depth contained a high Mn(II) fraction.

The third explanation is that glacial meltwater entering DI fjord initially contained Mn(II)-rich particles that are transformed to Mn(IV) by Mn(II)-oxidizing microorganisms populating the DI fjord water column. Although thermodynamically favourable, abiotic Mn(II) oxidation by O_2 is kinetically limited even in the presence of particle surfaces (Sung and Morgan, 1981). By contrast, biogenic Mn(II) oxidation is rapid, occurring on hour timescales (Sunda and Huntsman, 1987; Toner et al., 2005; Droz et al., 2015), and has been reported to produce Mn(IV)-bearing solids in freshwater and seawater with structures similar to the Mn(IV)-rich samples (Tebo et al., 2004; Webb et al., 2005). Once oxidized, Mn(IV)-rich particles are effective electron acceptors (Simanova and Pena, 2015), which, in addition to potential particle resuspension from the DI fjord floor (total depth of 120 m), can explain the decrease in AMOS at 90 m depth. One implication of the biogenic Mn(IV) production scenario is that this pathway suggests rapid Mn turnover and/or the oxidation of particulate Mn(II) since dMn was a small fraction of TdMn in these fjords. Although biogenic Mn(IV) production is most often reported for aqueous Mn(II), solid-phase Mn(II) oxidation is not unprecedented. For example, microbial-mediated oxidation of rhodochrosite ($MnCO_3$) has been shown to occur via microbial dissolution of mineral-hosted Mn(II) and subsequent oxidation by extracellular superoxide radicals (Tang et al., 2013).

The detection of Mn(IV)-rich particles in DI fjord is therefore interesting due to the unique redox and metal sorption reactivity of MnO_2, which can impact trace metal(loid) cycling in the water column (Tebo et al., 2004). Yet additional work is required to fully understand 1) the role and type of Mn(II) oxidizers, if present, in DI fjord and/or 2) the unique conditions favouring the presence of a Mn(IV) plume in DI fjord that are not present in the other investigated transects. One further potential caveat is that inner-fjord environments are dynamic interfaces in which ambient conditions, such as turbidity and water column structure, change markedly on both short-term (hours to days) and long-term (seasonal-interannual) timescales (Svendsen et al., 2002; De Andrés et al., 2020; Podolskiy et al., 2021). It therefore also remains an open question whether the Mn(IV) plume observed in DI fjord is a sustained feature, a seasonally recurring feature, or a sporadic feature appearing intermittently. While turbidity within the DI fjord is not atypical compared to the other systems herein, there is insufficient data to characterise seasonal evolution of this fjord compared to better studied systems such as GHF.

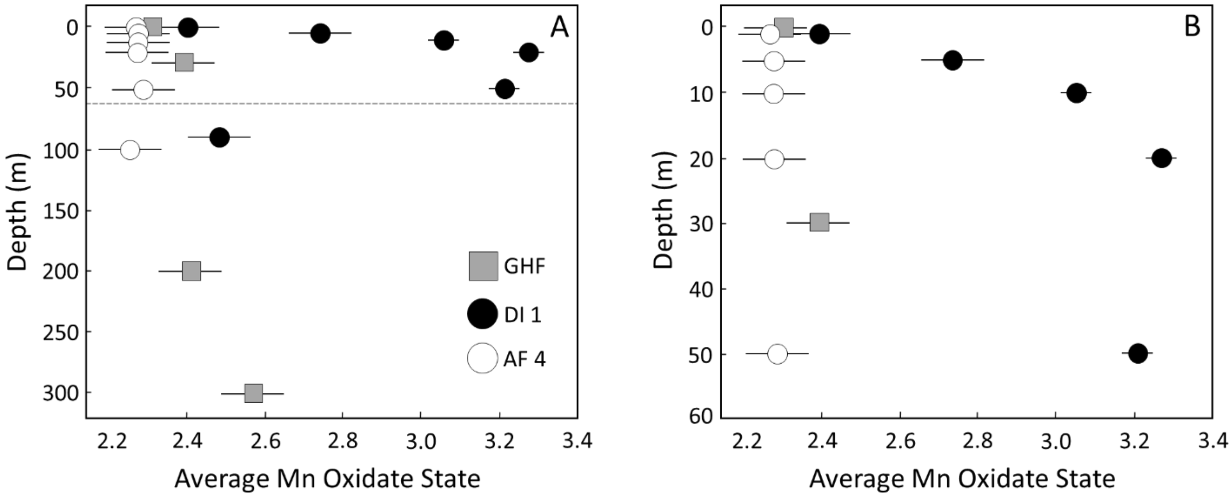

Figure 7: Change in average Mn oxidate state (AMOS) with depth for suspended particles obtained from Godthåbsfjord (GHF, grey squares), Disko Island (DI, black circles) and Arfersiorfik (AF, white circles). Panel B shows the upper-most 60 m of each depth profile, which is delineated by the grey dotted line in panel A.

5. Conclusions

Our study revealed that dMn concentrations were generally conservative across four different glacier fjord systems with contrasting geology and suspended particulate Mn speciation. Due to non-conservative removal of dFe at low salinities and low concentrations of dMn in freshwater relative to dFe, the dMn/dFe ratio increased at intermediate salinities (10-30) reflecting the higher stability of dMn. Mn(II)-rich phyllosilicates were widespread in suspended particles in fjord surface waters, but Mn(IV)-rich birnessite-like particles dominated at depths between 10 and 50 m in a fjord derived from tertiary basalt geology. These results imply the potential for a more complex redox cycle for suspended particulate Mn than Fe in glacially-modified fjords, especially at depths spanning the euphotic zone where the Mn oxidation state was observed to fluctuate in DI fjord, with biogenic Mn(II) oxidation speculated to be occurring in some inner-fjords. However, further investigations of microbiological populations in these inner-fjord environments is necessary to confirm the precise source of solid-phase Mn(IV). Considering the major differences in reactivity between Mn(II)-bearing phyllosilicates and birnessite-like Mn(IV), we hypothesize the distribution of biogeochemically-relevant trace elements, particularly metals with high sorption affinities for Mn oxides (e.g., Co, Ni, Zn and Pb), may be significantly altered in areas where Mn(IV)-rich suspended particles are prevalent. Our results provide an important insight into the geographical locations and depths where additional in-situ measurements of dissolved trace metals can help confirm this hypothesis.

Acknowledgements

We gratefully thank Ryan Davis at SSRL who facilitated collection of the Mn K-edge XAS data during virtual experiments imposed by COVID-19 travel restrictions. We acknowledge Alain Manceau for providing Mn reference spectra via an online database and Jasquelin Peña and her research group for useful discussions that improved the Mn K-edge XAS data interpretation. We also thank the three anonymous reviewers of this work who provided highly detailed and constructive reviews that improved the quality of our study. Use of SSRL, SLAC National Accelerator Laboratory, was supported by the U.S. Department of Energy, Office of Science, Basic Energy Sciences, under Contract No. DE-AC02- 607 76SF00515. This study formed part of project MarineGreen; Novo Nordic Foundation grant NNF17SH0028142. Mark Hopwood was financed by the DFG (award number HO 6321/1-1) and by the GLACE project, organised by the Swiss Polar Institute and supported by the Swiss Polar Foundation. T.L. was funded by the China Scholarship Council, and T.L. and J.K. were funded by GEOMAR. L.M. was funded by research programme VENI with project number 016.Veni.192.150, which is financed by the Dutch Research Council (NWO). We gratefully acknowledge the contributions from the Danish Centre for Marine Research (DCH), Greenland Institute of Natural Resources and the crew of RV Sanna for excellent field assistance. Thomas Juul-Pedersen (GINR) is thanked for assistance with fieldwork in Nuuk.

Research Data

In the Supplementary Materials (SM), we provide the tabulated dMn, TdMn and salinity measurements used to produce Figure 2 in Excel format and the dFe used to produce several figures. We also include in the Supplementary Materials the tabulated XANES, EXAFS and modelling fits in Excel format.

References

Achterberg E. P., Steigenberger S., Klar J. K., Browning T. J., Marsay C. M., Painter S. C., Vieira L. H., Baker A. R., Hamilton D. S., Tanhua T. and Moore C. M. (2021) Trace Element Biogeochemistry in the High-Latitude North Atlantic Ocean: Seasonal Variations and Volcanic Inputs. *Global Biogeochem. Cycles* **35**, 0–3.

Aciego S. M., Stevenson E. I. and Arendt C. A. (2015) Climate versus geological controls on glacial meltwater micronutrient production in southern Greenland. *Earth Planet. Sci. Lett.* **424**, 51–58. Available at: http://dx.doi.org/10.1016/j.epsl.2015.05.017.

De Andrés E., Slater D. A., Straneo F., Otero J., Das S. and Navarro F. (2020) Surface emergence of glacial plumes determined by fjord stratification. *Cryosphere* **14**, 1951–1969.

Ardiningsih I., Krisch S., Lodeiro P., Reichart G.-J., Achterberg E. P., Gledhill M., Middag R. and Gerringa L. J. A. (2020) Natural Fe-binding organic ligands in Fram Strait and over the northeast Greenland shelf. *Mar. Chem.* **224**.

Ball J. W. and Nordstrom D. K. (1991) User's Manual for WATEQ4F Database - US Geological Survey Open-File Report. , 91–183. Available at: https://pubs.usgs.gov/of/1991/0183/report.pdf%0Ahttp://wwwbrr.cr.usgs.gov/projects/GWC_chemtherm/pubs/wq4fdoc.pdf.

Bhatia M. P., Kujawinski E. B., Das S. B., Breier C. F., Henderson P. B. and Charette M. A. (2013) Greenland meltwater as a significant and potentially bioavailable source of iron to the ocean. *Nat. Geosci.* **6**, 274–278.

Boers N. and Rypdal M. (2021) Critical slowing down suggests that the western Greenland Ice Sheet is close to a tipping point. *Proc. Natl. Acad. Sci. U. S. A.* **118**, 1–7.

Boyd P. W. and Ellwood M. J. (2010) The biogeochemical cycle of iron in the ocean. *Nat. Geosci.* **3**, 675–682. Available at: http://dx.doi.org/10.1038/ngeo964.

Boyle E. A., Edmond J. M. and Sholkovitz E. R. (1977) The mechanism of iron removal in estuaries. *Geochim. Cosmochim. Acta* **41**, 1313–1324.

Browning T. J., Achterberg E. P., Engel A. and Mawji E. (2021) Manganese co-limitation of phytoplankton growth and major nutrient drawdown in the Southern Ocean. *Nat. Commun.* **12**, 1–9. Available at: http://dx.doi.org/10.1038/s41467-021-21122-6.

Carroll S., O'Day P. A., Esser B. and Randall S. (2002) Speciation and fate of trace metals in estuarine sediments under reduced and oxidized conditions, Seaplane Lagoon, Alameda Naval Air Station (USA). *Geochem. Trans.* **3**, 81–101.

Colombo M., Jackson S. L., Cullen J. T. and Orians K. J. (2020) Dissolved iron and manganese in the Canadian Arctic Ocean: On the biogeochemical processes controlling their distributions. *Geochim. Cosmochim. Acta* **277**, 150–174. Available at: https://doi.org/10.1016/j.gca.2020.03.012.

Davies S. H. R. and Morgan J. J. (1989) Manganese(II) Oxidation-Kinetics on Metal-Oxide Surfaces. *J. Colloid Interface Sci.* **129**, 63–77.

Dawes P. R. (2009) The bedrock geology under the Inland Ice: The next major challenge for Greenland mapping. *Geol. Surv. Denmark Greenl. Bull.*, 57–60.

Defoor W., Person M., Larsen H. C., Lizarralde D., Cohen D. and Dugan B. (2011) Ice sheet-derived submarine groundwater discharge on Greenland's continental shelf. *Water Resour. Res.* **47**.

Diem D. and Stumm W. (1984) Is dissolved Mn2+ being oxidized by O2 in absence of Mn-bacteria or surface catalysts? *Geochim. Cosmochim. Acta* **48**, 1571–1573.

Droz B., Dumas N., Duckworth O. W. and Peña J. (2015) A comparison of the sorption reactivity of bacteriogenic and mycogenic Mn oxide nanoparticles. *Environ. Sci. Technol.* **49**, 4200–4208.

Evans L. K. and Nishioka J. (2018) Quantitative analysis of Fe, Mn and Cd from sea ice and seawater in the Chukchi Sea, Arctic Ocean. *Polar Sci.* **17**, 50–58. Available at: https://doi.org/10.1016/j.polar.2018.07.002.

Forsch K., Hahn-Woernle L., Sherrell R. M., Roccanova J., Bu K., Burdige D., Vernet M. and Barbeau K. (2021) Seasonal dispersal of fjord meltwaters as an important source of iron to coastal Antarctic phytoplankton. *Biogeochemistry,* 1–52.

van Genuchten C. M. and Pena J. (2017) Mn(II) Oxidation in Fenton and Fenton Type Systems: Identification of Reaction Efficiency and Reaction Products. *Environ. Sci. Technol.* **51**, 2982–2991.

van Genuchten C. M., Rosing M. T., Hopwood M. J., Liu T., Krause J. and Meire L. (2021) Decoupling of particles and dissolved iron downstream of Greenlandic glacier outflows. *Earth Planet. Sci. Lett.* **576**, 117234. Available at: https://doi.org/10.1016/j.epsl.2021.117234.

Gledhill M. and Buck K. N. (2012) The organic complexation of iron in the marine environment: A review. *Front. Microbiol.* **3**, 1–17.

Goldberg E. D. (1954) Marine Geochemistry 1. Chemical Scavengers of the Sea. *J. Geol.* **62**, 249–265.

Grangeon S., Lanson B., Miyata N., Tani Y. and Manceau A. (2010) Structure of nanocrystalline phyllomanganates produced by freshwater fungi. *Am. Mineral.* **95**, 1608–1616.

Van Groeningen N., Glück B., Christl I. and Kretzschmar R. (2020) Surface precipitation of Mn2+on clay minerals enhances Cd2+sorption under anoxic conditions. *Environ. Sci. Process. Impacts* **22**, 1654–1665.

Hansel C. M. (2017) *Manganese in Marine Microbiology*. 1st ed., Elsevier Ltd. Available at: http://dx.doi.org/10.1016/bs.ampbs.2017.01.005.

Hartmann J., Dürr H. H., Moosdorf N., Meybeck M. and Kempe S. (2012) The geochemical composition of the terrestrial surface (without soils) and comparison with the upper continental crust. *Int. J. Earth Sci.* **101**, 365–376.

Hawco N. J., Lam P. J., Lee J. M., Ohnemus D. C., Noble A. E., Wyatt N. J., Lohan M. C. and Saito M. A. (2018) Cobalt scavenging in the mesopelagic ocean and its influence on global mass balance: Synthesizing water column and sedimentary fluxes. *Mar. Chem.* **201**, 151–166.

Hawkings J. R., Skidmore M. L., Wadham J. L., Priscu J. C., Morton P. L., Hatton J. E., Gardner C. B., Kohler T. J., Stibal M., Bagshaw E. A., Steigmeyer A., Barker J., Dore J. E., Berry Lyons W., Tranter M. and Spencer R. G. M. (2020) Enhanced trace element mobilization by Earth's ice sheets. *Proc. Natl. Acad. Sci. U. S. A.* **117**, 31648–31659.

Hopwood M. J., Connelly D. P., Arendt K. E., Juul-Pedersen T., Stinchcombe M. C., Meire L., Esposito M. and Krishna R. (2016) Seasonal changes in Fe along a glaciated Greenlandic fjord. *Front. Earth Sci.* **4**, 1–13.

Jensen L. T., Morton P., Twining B. S., Heller M. I., Hatta M., Measures C. I., John S., Zhang R., Pinedo-Gonzalez P., Sherrell R. M. and Fitzsimmons J. N. (2020) A comparison of marine Fe and Mn cycling: U.S. GEOTRACES GN01 Western Arctic case study. *Geochim. Cosmochim. Acta* **288**, 138–160. Available at: https://doi.org/10.1016/j.gca.2020.08.006.

Jones M. R., Luther G. W. and Tebo B. M. (2020) Distribution and concentration of soluble manganese(II), soluble reactive Mn(III)-L, and particulate MnO2 in the Northwest Atlantic Ocean. *Mar. Chem.* **226**, 103858. Available at: https://doi.org/10.1016/j.marchem.2020.103858.

Kandel A. and Aguilar-Islas A. (2021) Spatial and temporal variability of dissolved aluminum and manganese in surface waters of the northern Gulf of Alaska. *Deep. Res. Part II Top. Stud. Oceanogr.* **189**–**190**, 104952. Available at: https://doi.org/10.1016/j.dsr2.2021.104952.

Krause J., Hopwood M. J., Höfer J., Krisch S., Achterberg E. P., Alarcón E., Carroll D., González H. E., Juul-Pedersen T., Liu T., Lodeiro P., Meire L. and Rosing M. T. (2021) Trace Element (Fe, Co, Ni and Cu) Dynamics Across the Salinity Gradient in Arctic and Antarctic Glacier Fjords. *Front. Earth Sci.* **9**, 1–20.

Krisch S., Hopwood M. J., Schaffer J., Al-Hashem A., Höfer J., Rutgers van der Loeff M. M., Conway T. M., Summers B. A., Lodeiro P., Ardiningsih I., Steffens T. and Achterberg E. P. (2021) The 79°N Glacier cavity modulates subglacial iron export to the NE Greenland Shelf. *Nat. Commun.* **12**. Available at: http://dx.doi.org/10.1038/s41467-021-23093-0.

Langen P. L., Mottram R. H., Christensen J. H., Boberg F., Rodehacke C. B., Stendel M., van As D., Ahlstrøm A. P., Mortensen J., Rysgaard S., Petersen D., Svendsen K. H., Adalgeirsdóttir G. and Cappelen J. (2015) Quantifying energy and mass fluxes controlling Godthåbsfjord freshwater input in a 5-km simulation (1991-2012). *J. Clim.* **28**, 3694–3713.

Lanson B., Drits V. A., Feng Q. and Manceau A. (2002) Structure of synthetic Na-birnessite: Evidence for a triclinic one-layer unit cell. *Am. Mineral.* **87**, 1662–1671.

Latour P., Wuttig K., van der Merwe P., Strzepek R. F., Gault-Ringold M., Townsend A. T., Holmes T. M., Corkill M. and Bowie A. R. (2021) Manganese biogeochemistry in the Southern Ocean, from Tasmania to Antarctica. *Limnol. Oceanogr.*

Learman D. R., Voelker B. M., Madden A. S. and Hansel C. M. (2013) Constraints on superoxide mediated formation of manganese oxides. *Front. Microbiol.* **4**.

Learman D. R., Wankel S. D., Webb S. M., Martinez N., Madden A. S. and Hansel C. M. (2011) Coupled biotic-abiotic Mn(II) oxidation pathway mediates the formation and structural evolution of biogenic Mn oxides. *Geochim. Cosmochim. Acta* **75**, 6048–6063.

Lefebvre P., Gourgiotis A., Mangeret A., Sabatier P., Le Pape P., Diez O., Louvat P., Menguy N., Merrot P., Baya C., Zebracki M., Blanchart P., Malet E., Jezequel D., Reyss J.-L., Bargar J. R., Gaillardet J., Cazala C. and Morin G. (2021) Diagenetic formation of uranium-silica polymers in lake sediments over 3,300 years. *Proc. Natl. Acad. Sci. U. S. A.* **118**.

Lenz C., Behrends T., Jilbert T., Silveira M. and Slomp C. P. (2014) Redox-dependent changes in manganese speciation in Baltic Sea sediments from the Holocene Thermal Maximum: An EXAFS, XANES and LA-ICP-MS study. *Chem. Geol.* **370**, 49–57.

Lewis E. L. and Perkin R. G. (1978) Salinity: Its definition and calculation. *J. Geophys. Res.* **83**, 466.

Ling F. T., Post J. E., Heaney P. J. and Ilton E. S. (2018) The relationship between Mn oxidation state and structure in triclinic and hexagonal birnessites. *Chem. Geol.* **479**, 216–227. Available at: https://doi.org/10.1016/j.chemgeo.2018.01.011.

Malinowski E. R. (1977) Determination of the Number of Factors and the Experimental Error in a Data Matrix. *Anal. Chem.* **49**, 612–617.

Manceau A., Marcus M. A. and Grangeon S. (2012) Determination of Mn valence states in mixed-valent manganates by XANES spectroscopy. *Am. Mineral.* **97**, 816–827.

Mankoff K. D., Noël B., Fettweis X., Ahlstrøm A. P., Colgan W., Kondo K., Langley K., Sugiyama S., Van As D. and Fausto R. S. (2020) Greenland liquid water discharge from 1958 through 2019. *Earth Syst. Sci. Data* **12**, 2811–2841.

Marafatto F. F., Strader M. L., Gonzalez-Holguera J., Schwartzberg A., Gilbert B., Peña J. and Pena J. (2015) Rate and mechanism of the photoreduction of birnessite (MnO2) nanosheets. *Proc. Natl. Acad. Sci. U. S. A.* **112**, 4600–4605. Available at: https://www.ncbi.nlm.nih.gov/pubmed/25825757.

Mascarenhas V. J. and Zielinski O. (2019) Hydrography-driven optical domains in the Vaigat-Disko Bay and Godthabsfjord: Effects of glacial meltwater discharge. *Front. Mar. Sci.* **6**, 1–19.

Matsunaga K., Ohyama T., Kuma K., Kudo I. and Suzuki Y. (1995) Photoreduction of manganese dioxide in seawater by organic substances under ultraviolet or sunlight. *Water Res.* **29**, 757–759.

Mendez J., Guieu C. and Adkins J. (2010) Atmospheric input of manganese and iron to the ocean: Seawater dissolution experiments with Saharan and North American dusts. *Mar. Chem.* **120**, 34–43. Available at: http://dx.doi.org/10.1016/j.marchem.2008.08.006.

Morel F. M. M. and Price N. M. (2003) The biogeochemical cycles of trace metals in the oceans. *Science (80-.).* **300**, 944–947.

Morgan J. J. (2005) Kinetics of reaction between O-2 and Mn(II) species in aqueous solutions. *Geochim. Cosmochim. Acta* **69**, 35–48.

Mortensen J., Bendtsen J., Lennert K. and Rysgaard S. (2014) Seasonal variability of the circulation system in a west Greenland tidewater outlet glacier fjord, Godthåbsfjord (64°N). *J. Geophys. Res. Earth Surf.* **119**, 2591–2603.

Mortensen J., Lennert K., Bendtsen J. and Rysgaard S. (2011) Heat sources for glacial melt in a sub-Arctic fjord (Godthåbsfjord) in contact with the Greenland Ice Sheet. *J. Geophys. Res. Ocean.* **116**.

Naeraa T., Kemp A. I. S., Schersten A., Rehnstrom E., Rosing M. T. and Whitehouse M. J. (2014) A lower crustal mafic source for the ca. 2550 Ma Qorqut Granite Complex in southern West Greenland. *Lithos* **192**, 291–304.

Nelson W. R. and Griffen D. T. (2005) Crystal chemistry of Zn-rich rhodonite (“fowlerite”). *Am. Mineral.* **90**, 969–983.

Newville M. (2001) IFEFFIT: interactive XAFS analysis and FEFF fitting. *J. Synchrotron Radiat.*, 322–324.

Nico P. S., Anastasio C. and Zasoski R. J. (2002) Rapid photo-oxidation of Mn(II) mediated by humic substances. *Geochim. Cosmochim. Acta* **66**, 4047–4056.

Noble A. E., Moran D. M., Allen A. E. and Saito M. A. (2013) Dissolved and particulate trace metal micronutrients under the McMurdo Sound seasonal sea ice: Basal sea ice communities as a capacitor for iron. *Front. Chem.* **1**.

Oldham V. E., Lamborg C. H. and Hansel C. M. (2020) The Spatial and Temporal Variability of Mn Speciation in the Coastal Northwest Atlantic Ocean. *J. Geophys. Res. Ocean.* **125**.

Ostwald J. and Frazer F. W. (1973) Chemical and mineralogical investigations on deep sea manganese nodules from the Southern Ocean. *Miner. Depos.* **8**, 303–311.

Overeem I., Hudson B. D., Syvitski J. P. M., Mikkelsen A. B., Hasholt B., van den Broeke M. R., Noël B. P. Y. and Morlighem M. (2017) Substantial export of suspended sediment to the global oceans from glacial erosion in Greenland. *Nat. Geosci.* **10**, 859–863.

Pausch F., Bischof K. and Trimborn S. (2019) Iron and manganese co-limit growth of the Southern Ocean diatom Chaetoceros debilis. *PLoS One* **14**, 1–16.

Peers G. and Price N. M. (2004) A role for manganese in superoxide dismutases and growth of iron-deficient diatoms. *Limnol. Oceanogr.* **49**, 1774–1783.

Podolskiy E. A., Kanna N. and Sugiyama S. (2021) Co-seismic eruption and intermittent turbulence of a subglacial discharge plume revealed by continuous subsurface observations in Greenland. *Commun. Earth Environ.* **2**, 1–16. Available at: http://dx.doi.org/10.1038/s43247-021-00132-8.

Proux O., Lahera E., Del Net W., Kieffer I., Rovezzi M., Testemale D., Irar M., Thomas S., Aguilar-Tapia A., Bazarkina E. F., Prat A., Tella M., Auffan M., Rose J. and Hazemann J.-L. (2017) High-Energy Resolution Fluorescence Detected X-Ray Absorption Spectroscopy: A Powerful New Structural Tool in Environmental Biogeochemistry Sciences. *J. Environ. Qual.* **46**, 1146–1157.

Rapp I., Schlosser C., Rusiecka D., Gledhill M. and Achterberg E. P. (2017) Automated preconcentration of Fe, Zn, Cu, Ni, Cd, Pb, Co, and Mn in seawater with analysis using high-resolution sector field inductively-coupled plasma mass spectrometry. *Anal. Chim. Acta* **976**, 1–13. Available at: http://dx.doi.org/10.1016/j.aca.2017.05.008.

Schlitzer R. (2014) Ocean Data View. http://odv.awi.de.

Simanova A. A. and Pena J. (2015) Time-resolved investigation of cobalt oxidation by Mn(III)-rich d-MnO2 using quick X-ray absorption spectroscopy. *Environ. Sci. Technol.*

Slater T., Shepherd A., McMillan M., Leeson A., Gilbert L., Muir A., Munneke P. K., Noël B., Fettweis X., van den Broeke M. and Briggs K. (2021) Increased variability in Greenland Ice Sheet runoff from satellite observations. *Nat. Commun.* **12**, 1–9. Available at: http://dx.doi.org/10.1038/s41467-021-26229-4.

Statham P. J., Skidmore M. and Tranter M. (2008) Inputs of glacially derived dissolved and colloidal iron to the coastal ocean and implications for primary productivity. *Global Biogeochem. Cycles* **22**, n/a-n/a.

Stevenson E. I., Fantle M. S., Das S. B., Williams H. M. and Aciego S. M. (2017) The iron isotopic composition of subglacial streams draining the Greenland ice sheet. *Geochim. Cosmochim. Acta* **213**, 237–254. Available at: http://dx.doi.org/10.1016/j.gca.2017.06.002.

Straneo F. and Cenedese C. (2015) The dynamics of greenland's glacial fjords and their role in climate. *Ann. Rev. Mar. Sci.* **7**, 89–112.

Sunda W. G. (2012) Feedback interactions between trace metal nutrients and phytoplankton in the ocean. *Front. Microbiol.* **3**.

Sunda W. G. and Huntsman S. A. (1988) Effect of sunlight on redox cycles of manganese in the southwestern Sargasso Sea. *Deep Sea Res. Part A, Oceanogr. Res. Pap.* **35**, 1297–1317.

Sunda W. G. and Huntsman S. A. (1987) Microbial oxidation of manganese in a North Carolina estuary. *Limnol. Oceanogr.* **32**, 552–564.

Sunda W. G., Huntsman S. A. and Harvey G. R. (1983) Photoreduction of manganese oxides in seawater and its geochemical and biological implications. *Nature* **301**, 234–236.

Sung W. and Morgan J. J. (1981) Oxidative removal of Mn(II) from solution catalyzed by the gamma FeOOH (lepidocrocite) surface. *Geochim. Cosmochim. Acta* **45**, 2377–2383.

Svendsen H., Beszczynska-Møller A., Hagen J. O., Lefauconnier B., Tverberg V., Gerland S., Børre Ørbæk J., Bischof K., Papucci C., Zajaczkowski M., Azzolini R., Bruland O. and Wiencke C. (2002) The physical environment of Kongsfjorden–Krossfjorden, an Arctic fjord system in Svalbard. *Polar Res.* **21**, 133–166.

Tang Y., Zeiner C. A., Santelli C. M. and Hansel C. M. (2013) Fungal oxidative dissolution of the Mn(II)-bearing mineral rhodochrosite and the role of metabolites in manganese oxide formation. *Environ. Microbiol.* **15**, 1063–1077.

Tebo B. M., Bargar J. R., Clement B. G., Dick G. J., Murray K. J., Parker D., Verity R. and Webb S. M. (2004) Biogenic manganese oxides: Properties and mechanisms of formation. *Annu. Rev. Earth Planet. Sci.* **32**, 287–328.

Tebo B. M. and Emerson S. (1986) Microbial manganese(II) oxidation in the marine environment: a quantitative study. *Biogeochemistry* **2**, 149–161.

Toner B., Fakra S., Villalobos M., Warwick T. and Sposito G. (2005) Spatially Resolved Characterization of Biogenic Manganese Oxide Production within a Bacterial Biofil. *Appl. Environ. Microbiol.* **71**, 1300–1310.

Wang Y. and Stone A. T. (2006) The citric acid-Mn(III,IV)O(2)(birnessite) reaction. Electron transfer, complex formation, and autocatalytic feedback. *Geochim. Cosmochim. Acta* **70**, 4463–4476.

Webb S. (2005) SIXPACK: a graphical user interface for XAS analysis using IFEFFIT. *Phys. Scr.* **T115**, 1011–1014.

Webb S. M., Tebo B. M. and Bargar J. R. (2005) Structural characterization of biogenic Mn oxides produced in seawater by the marine bacillus sp. strain SG-1. *Am. Mineral.* **90**, 1342–1357.

Wehrmann L. M., Formolo M. J., Owens J. D., Raiswell R., Ferdelman T. G., Riedinger N. and Lyons T. W. (2014) Iron and manganese speciation and cycling in glacially influenced high-latitude fjord sediments (West Spitsbergen, Svalbard): Evidence for a benthic recycling-transport mechanism. *Geochim. Cosmochim. Acta* **141**, 628–655. Available at: http://dx.doi.org/10.1016/j.gca.2014.06.007.

Wyckoff R. W. G. (1963) Crystal Structures. **1**, 290–295.

Xiang Y. and Lam P. J. (2020) *Size-Fractionated Compositions of Marine Suspended Particles in the Western Arctic Ocean: Lateral and Vertical Sources*.,

Xiang Y., Lam P. J. and Lee J.-M. (2021) Diel redox cycle of manganese in the surface Arctic Ocean. , 1–25. Available at: http://www.essoar.org/doi/10.1002/essoar.10507350.1.

Yamazaki S. and Toraya H. (1999) Rietveld refinement of site-occupancy parameters of Mg2-xMnxSiO4 using a new weight function in least-squares fitting. *J. Appl. Crystallogr.* **32**, 51–59.

Yu C., Virtasalo J. J., Österholm P., Burton E. D., Peltola P., Ojala A. E. K., Hogmalm J. K. and Åström M. E. (2016) Manganese accumulation and solid-phase speciation in a 3.5 m thick mud sequence from the estuary of an acidic and Mn-rich creek, northern Baltic Sea. *Chem. Geol.* **437**, 56–66. Available at: http://dx.doi.org/10.1016/j.chemgeo.2016.05.016.

Yu Q., Sasaki K., Tanaka K., Ohnuki T. and Hirajima T. (2012) Structural factors of biogenic birnessite produced by fungus Paraconiothyrium sp. WL-2 strain affecting sorption of Co 2+. *Chem. Geol.* **310**–**311**, 106–113. Available at: http://dx.doi.org/10.1016/j.chemgeo.2012.03.029.

Zhang T., Liu L., Tan W., Suib S. L., Qiu G. and Liu F. (2018) Photochemical Formation and Transformation of Birnessite: Effects of Cations on Micromorphology and Crystal Structure. *Environ. Sci. Technol.* **52**, 6864–6871.

Zhu M. Q., Farrow C. L., Post J. E., Livi K. J. T., Billinge S. J. L., Ginder-Vogel M. and Sparks D. L. (2012) Structural study of biotic and abiotic poorly-crystalline manganese oxides using atomic pair distribution function analysis. *Geochim. Cosmochim. Acta* **81**, 39–55.